J. Fluid Mech. (2021), *vol*. 922, A3, doi:10.1017/jfm.2021.490

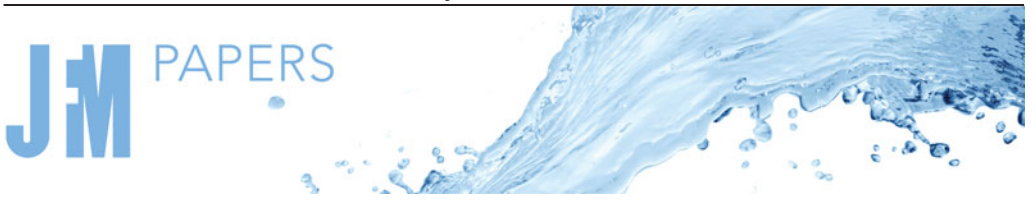

On the role of vorticity stretching and strain self-amplification in the turbulence energy cascade

Perry L. Johnson†

Department of Mechanical and Aerospace Engineering, University of California, Irvine, CA, USA

(Received 7 February 2021; revised 26 April 2021; accepted 27 May 2021)

The tendency of turbulent flows to produce fine-scale motions from large-scale energy injection is often viewed as a scale-wise cascade of kinetic energy driven by vorticity stretching. This has been recently evaluated by an exact, spatially local relationship (Johnson, P.L. *Phys. Rev. Lett.*, vol. 124, 2020, p. 104501), which also highlights the contribution of strain self-amplification. In this paper, the role of these two mechanisms is explored in more detail. Vorticity stretching and strain amplification interactions between velocity gradients filtered at the same scale account for approximately half of the energy cascade rate, directly connecting the restricted Euler dynamics to the energy cascade. Multiscale strain amplification and vorticity stretching are equally important, however, and more closely resemble eddy viscosity physics. Moreover, ensuing evidence of a power-law decay of energy transfer contributions from disparate scales supports the notion of an energy cascade, albeit a 'leaky' one. Besides vorticity stretching and strain self-amplification, a third mechanism of energy transfer is introduced and related to the vortex thinning mechanism important for the inverse cascade in two dimensions. Simulation results indicate this mechanism also provides a net source of backscatter in three-dimensional turbulence, in the range of scales associated with the bottleneck effect. Taken together, these results provide a rich set of implications for large-eddy simulation modelling.

Key words: turbulent flows

1. Introduction

One of the most salient features of turbulent flows is enhanced rates of energy dissipation (ϵ) and mixing. Turbulence rapidly produces fine-scale variations in the velocity field. The dynamics of this process has been of enduring interest for understanding and modelling turbulent flows across a wide range of applications. The resulting broadband range of

† Email address for correspondence: perry.johnson@uci.edu

length and time scales, evolving under intrinsically nonlinear dynamics, lies at the centre of what makes turbulent flows challenging to analyse, model and predict.

The kinetic energy cascade is the predominant concept for illuminating the production of small scales in turbulence (Richardson 1922; Kolmogorov 1941*b*; Onsager 1949; Frisch 1995). Turbulent kinetic energy is produced primarily in the form of large-scale motions with size comparable to that of the shear flow that serves as the energy source. The kinetic energy is dissipated to thermal energy by viscosity (ν) primarily acting on the smallest-scale motions in the flow, which are comparable in size to the Kolmogorov length scale, $\eta = \nu^{3/4}\epsilon^{-1/4}$ (Kolmogorov 1941*b*). The energy cascade describes the process of transferring kinetic energy from the largest-scale motions where it is produced to the smallest-scale motions responsible for irreversible dissipation. The cascade phenomenology asserts that the predominant exchanges of energy occur between coherent motions having nearly the same size, so that energy is passed in a quasi step-wise manner to successively smaller-scale motions. The cascade terminates when the smallest scales are finally energized and viscous dissipation removes kinetic energy at the rate it is supplied.

The energy cascade provides a conceptually simple phenomenological explanation for the observed complex, chaotic behaviour of turbulence. Supposing that the energy transfer processes are chaotic and somewhat independent across length scales, the cascade idea provides an attractive explanation for why universal properties are observed for such a wide range of turbulent flow scenarios. However, two significant questions are raised.

First, is the net transfer of energy from large to small scales in turbulence actually accomplished primarily by interactions between motions having nearly the same size? This is the question of scale locality, which is a necessary property for the cascade phenomenology to be plausible. Strictly speaking, the energy transfer does not occur in a well-defined step-like manner (Lumley 1992). In this sense, the cascade is 'leaky'. However, the question of scale locality may be answered more rigorously by quantifying the relative contribution of interactions between differently sized motions to the energy cascade rate. Theoretical analysis predicts that the contribution to the cascade rate across scale ℓ due to interactions with motions at scale $\ell' < \ell$ decays as a power law for $\ell' \ll \ell$, specifically, $\sim(\ell'/\ell)^{4/3}$ (Kraichnan 1966, 1971; Eyink 2005; Eyink & Aluie 2009). This power law indicates the degree of ultra-violet locality (L'vov & Falkovich 1992). Numerous numerical investigations have revealed at least some degree of scale locality in the mean energy transfer across scales, with general support for the theoretical scaling (Zhou 1993*a*,*b*; Aoyama *et al.* 2005; Mininni, Alexakis & Pouquet 2006; Domaradzki & Carati 2007*a*,*b*; Mininni, Alexakis & Pouquet 2008; Aluie & Eyink 2009; Domaradzki, Teaca & Carati 2009; Eyink & Aluie 2009; Cardesa *et al.* 2015; Doan *et al.* 2018).

The second question of significant importance to the energy cascade phenomenology is: What dynamical mechanism is responsible for driving such a cascade? To some degree, answering this second question should also shed some light on the first. That is, identifying the dynamical mechanism of the cascade should provide some basis for examining the scale locality of that mechanism. For example, consider the most commonly cited mechanism for the cascade, i.e. vortex stretching (Taylor 1938; Onsager 1949; Tennekes & Lumley 1972). The vortex stretching mechanism of the energy cascade is illustrated in figure 1 and may be described as follows. A compact region characterized by elevated vorticity (i.e. a vortex) subjected to an extensional strain rate along its axis of rotation will have its cross-section reduced. As this occurs, the vorticity in that region will be enhanced in keeping with Kelvin's theorem. In this way, kinetic energy is passed from straining motions to vortical motions that decrease in size. Owing to this proposed

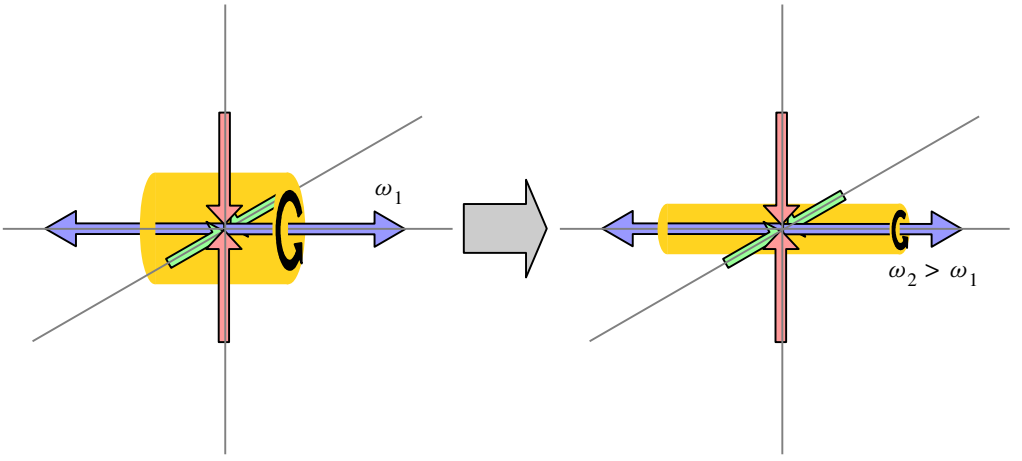

Figure 1. A simplified illustration of vortex stretching.

cascade mechanism, the role of vortex structures in turbulence dynamics has been an active subject of research over the years (Lundgren 1982; Chorin 1988; Pullin & Saffman 1994, 1998; Jiménez & Wray 1998; Lozano-Durán, Holzner & Jiménez 2016). For instance, numerical simulations have been used to confirm that interactions between vortices and straining regions are strongest when the vortical structure is only somewhat smaller than the straining region (Doan *et al.* 2018).

The question of dynamical mechanism is of high importance in its own right (Carbone & Bragg 2020). This is especially true for reduced-order models of turbulence, a practical step for predicting many turbulent flows. Large-eddy simulations (LES) are widely used and increasing in popularity with growing computational resources. The LES approach directly calculates the dynamics of large-scale motions on a computational grid while requiring a closure model for representing the effect of smaller, unresolved scales on the computed large-scale motions. Arguably the most important feature of an LES closure model is that it removes energy from the resolved scales in an accurate manner. However, eddy viscosity closures remain the most common approach to LES alongside heuristic approaches which rely on implicit modelling via specially designed discretization errors. From a physical perspective, these popular models are known to be deficient despite their widespread use (Borue & Orszag 1998). In contrast, the stretched vortex model of Misra & Pullin (1997) attempts to build a model on more explicit physical grounds, appealing to the classical vortex stretching mechanism of the cascade. It has also been proposed to use vortex stretching to determine an eddy viscosity (Silvis & Verstappen 2019).

More recently, the self-amplification of straining motions has been proposed as an alternative cascade mechanism (Tsinober 2009; Paul, Papadakis & Vassilicos 2017; Carbone & Bragg 2020; Johnson 2020*a*), casting doubt on the widespread view that the cascade is driven primarily by vortex stretching. Strain-rate self-amplification is illustrated in figure 2. A region of enhanced strain rate with one strong negative eigenvalue experiences a strengthening of that compressive strain rate as faster moving fluid catches up with slower moving fluid in front of it. This decreases the spatial extent of strong compressive strain rate. This mechanism is responsible for the finite-time singularity and shock formation in the inviscid Burgers equation, but has received much less attention in the context of Navier–Stokes. The restricted Euler equation, a dynamical system more relevant to three-dimensional (3-D) Navier–Stokes than the Burgers equation, displays a

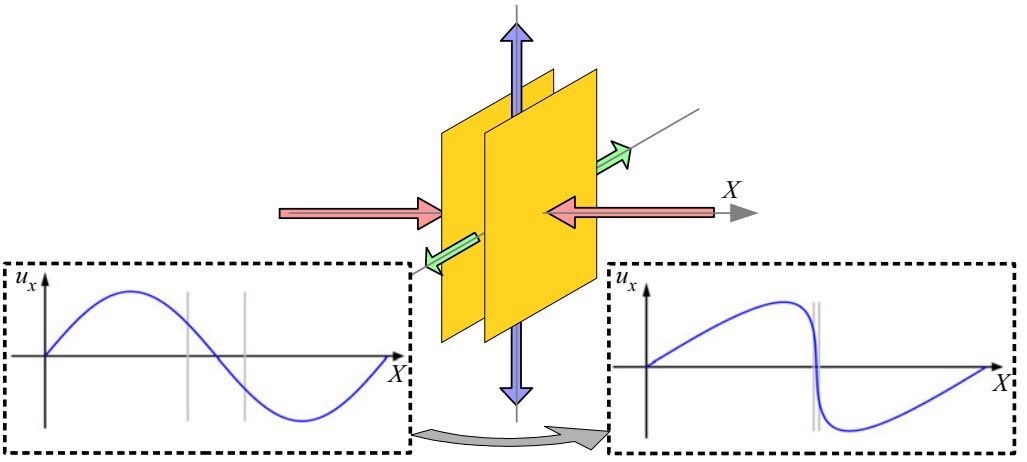

Figure 2. A simplified schematic of strain self-amplification.

finite-time singularity that includes both strain self-amplification and vorticity stretching (Vieillefosse 1982).

Indeed, more careful accounting of the relative contributions of vortex stretching and strain self-amplification in turbulent flows indicate that the latter is responsible for a larger share of the energy cascade rate. Most notably, Johnson (2020*a*) derived an exact, spatially local relationship between the energy cascade rate and the dynamical mechanisms of vortex stretching and strain self-amplification. It is the goal of this paper to leverage this result to illuminate key aspects of the cascade as seen from the perspective of velocity gradient dynamics.

In this paper, the roles of vortex stretching and strain self-amplification in determining the energy cascade rate are elucidated. First, § 2 reviews turbulent velocity gradients dynamics and the framework for studying the energy cascade in terms of spatial filtering. The connection between the velocity gradients and the cascade is established in § 3, enhancing and building upon the results of Johnson (2020*a*). Simulation results highlight the relative importance of each mechanism to the energy cascade. Also included is a brief discussion of the inverse energy cascade in 2-D flows, demonstrating a comprehensive framework for turbulent cascades. Following that, § 4 builds on the concept of cascade efficiency from Ballouz & Ouellette (2018), examining the efficiency of the dynamical mechanisms comprising the cascade rate. This analysis reveals the relevance of the restricted Euler dynamics to the energy cascade, while judging the relative suitability of an eddy viscosity hypothesis for representing the various dynamical processes involved. Then, § 5 returns to the question of scale locality in terms of both vorticity stretching and strain self-amplification. It is shown that the concept of cascade efficiency can be examined on a scale-by-scale basis to test the de-correlation idea of Eyink (2005). Conclusions are drawn in § 6.

2. Background

2.1. *Simulation database: homogeneous isotropic turbulence*

In this paper, the kinetic energy cascade is quantified via direct numerical simulation (DNS) of forced homogeneous isotropic turbulence (HIT) in a triply periodic domain.

The incompressible Navier–Stokes equations,

$$\frac{\partial u_i}{\partial t} + u_j \frac{\partial u_i}{\partial x_j} = -\frac{\partial p}{\partial x_i} + \nu \nabla^2 u_i + f_i, \quad \frac{\partial u_j}{\partial x_j} = 0, \tag{2.1a,b}$$

are solved using a pseudo-spectral method with 1024 collocation points in each direction. The velocity field, $\boldsymbol{u}$, is advanced in time with a second-order Adams–Bashforth scheme, and the pressure p simply enforces the divergence-free condition. The $2\sqrt{2}/3$ rule for wavenumber truncation is used with phase-shift dealiasing (Patterson & Orszag 1971). The forcing, $\boldsymbol{f}$, is specifically designed to maintain constant kinetic energy in the first two wavenumber shells. After a startup period, statistics are computed over 6 large-eddy turnover times. The Taylor-scale Reynolds number is approximately $Re_\lambda = 400$ with grid resolution $k_{max}\eta = 1.4$. The integral length scale is $L/\eta = 460$.

HIT is a very useful canonical flow to efficiently explore the energetics of small- and intermediate-scale turbulence dynamics. The analysis performed in this paper is not limited to HIT in principle, and the inertial range results are expected to be representative of a wide range of turbulent shear flows at sufficiently high Reynolds numbers.

2.2. *Velocity gradient tensor*

Vorticity stretching and strain self-amplification are dynamical processes defined via the velocity gradient tensor, $\boldsymbol{A}$, which is comprised of the strain-rate tensor, $\boldsymbol{S}$, and the rotation-rate tensor, $\boldsymbol{\Omega}$,

$$A_{ij} = \frac{\partial u_i}{\partial x_j} = S_{ij} + \Omega_{ij}, \quad S_{ij} = \frac{1}{2}(A_{ij} + A_{ji}), \quad \Omega_{ij} = \frac{1}{2}(A_{ij} - A_{ji}), \tag{2.2a–c}$$

where the rotation-rate tensor may be written in terms of the vorticity vector $\boldsymbol{\omega} = \nabla \times \boldsymbol{u}$,

$$\Omega_{ij} = -\tfrac{1}{2}\epsilon_{ijk}\omega_k, \quad \omega_i = -\epsilon_{ijk}\Omega_{jk}. \tag{2.3a,b}$$

This decomposition is foundational to the energetics of turbulent flows because viscosity resists deformation but not rotation. Thus, the rate at which kinetic energy is dissipated into thermal energy depends only on the (Frobenius norm of the) strain-rate tensor,

$$\epsilon = 2\nu S_{ij} S_{ij} = 2\nu \|\boldsymbol{S}\|^2. \tag{2.4}$$

On the other hand, the vorticity plays no direct role in the viscous dissipation of kinetic energy. However, vorticity is still essential to the dynamics leading to energy dissipation, as seen from the first relation of Betchov (1956) for incompressible homogeneous turbulence,

$$\langle \|\boldsymbol{S}\|^2 \rangle = \tfrac{1}{2}\langle |\boldsymbol{\omega}|^2 \rangle. \tag{2.5}$$

Angle brackets denote ensemble averaging. The Betchov relation shows that the average (or global) amount of vorticity and strain rate is held in balance for incompressible flows, presumably by the action of the pressure as it enforces $\nabla \cdot \boldsymbol{u} = 0$. Thus, the significantly enhanced dissipation rates in turbulence cannot occur without equally enhanced enstrophy. At sufficiently high Reynolds numbers, this relationship holds to good approximation even for inhomogeneous flows.

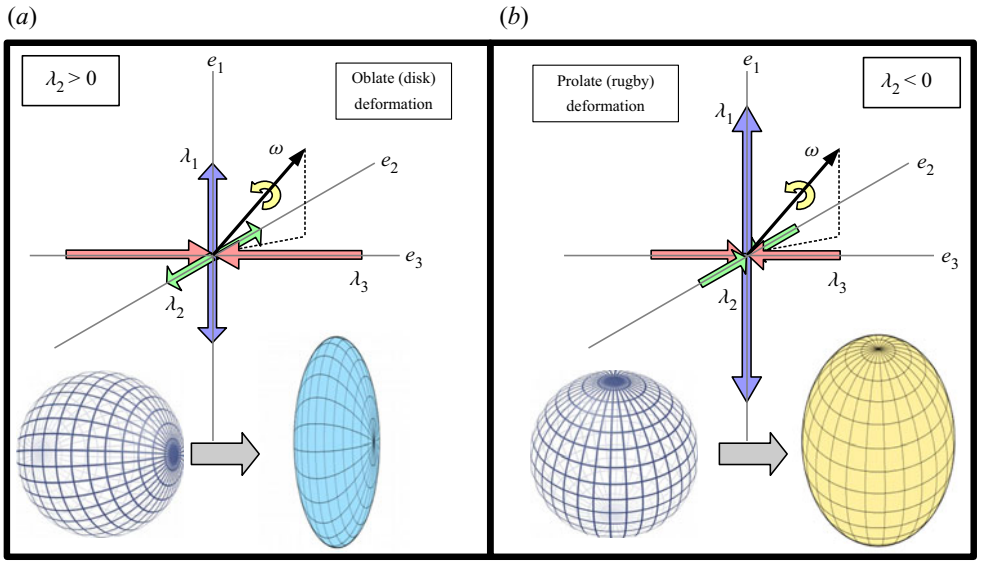

Figure 3. Depiction of the velocity gradient tensor in the strain-rate eigenframe. Velocity gradients with two extensional eigenvalues (*a*) tend to deform initially spherical fluid particles into disk-like oblate spheroids. Velocity gradients with two compressive eigenvalues (*b*) deform spherical fluid particles to prolate spheroids, like a rugby ball shape.

Similarly, the norm of the velocity gradient is the sum of the vorticity and strain-rate norms,

$$\tfrac{1}{2}\|\boldsymbol{A}\|^2 = \tfrac{1}{4}|\boldsymbol{\omega}|^2 + \tfrac{1}{2}\|\boldsymbol{S}\|^2, \tag{2.6}$$

so that (2.5) implies a statistical equi-partition between enstrophy and dissipation. Thus, the second invariant of the velocity gradient tensor,

$$Q = -\tfrac{1}{2}A_{ij}A_{ji} = \tfrac{1}{4}|\boldsymbol{\omega}|^2 - \tfrac{1}{2}\|\boldsymbol{S}\|^2, \tag{2.7}$$

has an average of zero.

The strain-rate tensor, being symmetric, has 3 real eigenvalues, $\lambda_1 > \lambda_2 > \lambda_3$, associated with a set of orthogonal eigenvectors. The eigenvalues sum to zero for incompressible flows, $\lambda_1 + \lambda_2 + \lambda_3 = 0$. Therefore, the largest eigenvalue is always extensional along its eigenvector, $\lambda_1 \geq 0$, and the smallest one is always compressive, $\lambda_3 \leq 0$. The intermediate eigenvalue, λ_2, may be positive or negative. The sign of λ_2 indicates the topology of fluid particle deformations, figure 3, and has more important dynamical effects as discussed below.

2.3. *Velocity gradient dynamics*

Consider a Lagrangian view of turbulence as a collection of fluid particles characterized by their deformational and rotational behaviour, i.e. their velocity gradient tensor. The Lagrangian evolution equation for the velocity gradient tensor is derived as the gradient of (2.1*a*,*b*),

$$\frac{\mathrm{D}A_{ij}}{\mathrm{D}t} = \underbrace{-A_{ik}A_{kj} - \frac{2}{3}Q\delta_{ij}}_{\textit{autonomous dynamics}} - \underbrace{\iiint_{PV}\left[\frac{Q(\boldsymbol{x}+\boldsymbol{r})}{2\pi|\boldsymbol{r}|^3}\left(\delta_{ij} - 3\frac{r_i r_j}{|\boldsymbol{r}|^2}\right)\right]\mathrm{d}\boldsymbol{r} + \nu\nabla^2 A_{ij}}_{\textit{nearby particle interactions}}, \tag{2.8}$$

where the formal solution of the pressure Poisson equation, $\nabla^2 p = 2Q$, is used to write the pressure Hessian as the sum of the second and third terms in (2.8) (Ohkitani & Kishiba 1995). The contribution of pressure to the autonomous dynamics is due to the enforcement of $\boldsymbol{\nabla \cdot u} = 0$ at the point on the trajectory, while the non-local integral arises from the enforcement of $\boldsymbol{\nabla \cdot u} = 0$ at all surrounding points. For HIT simulations with large-scale forcing, the gradient of the force is typically negligible compared to other terms in (2.8) at high Reynolds numbers.

Significant insight may be gained into velocity gradient dynamics by focusing only on its autonomous dynamics using the restricted Euler equation,

$$\frac{\mathrm{D}A_{ij}}{\mathrm{D}t} = -A_{ik}A_{kj} - \frac{1}{3}A_{mn}A_{nm}\delta_{ij}. \tag{2.9}$$

By neglecting the interaction with the velocity gradients of other surrounding fluid particles, the restricted Euler equation represents a dramatic mathematical simplification of turbulent flows while retaining some key dynamical processes. In fact, rigorous mathematical results are possible (Vieillefosse 1982, 1984; Cantwell 1992).

The most salient feature of solutions to the restricted Euler equation is a finite-time singularity for (almost) all initial conditions. The cause of this singularity may be readily identified using the equation for the velocity gradient norm in restricted Euler dynamics,

$$\frac{\mathrm{D}}{\mathrm{D}t}\left(\frac{1}{2}\|\boldsymbol{A}\|^2\right) = \underbrace{\frac{1}{4}\omega_i S_{ij}\omega_j}_{P_\omega} - \underbrace{S_{ij}S_{jk}S_{ki}}_{P_s}. \tag{2.10}$$

The two terms on the right side of (2.10) represent production of velocity gradient magnitude by vorticity stretching and strain self-amplification, respectively.

The local rate of velocity gradient production by vorticity stretching/compression,

$$P_\omega = \tfrac{1}{4}|\boldsymbol{\omega}|^2 \sum_{i=1}^{3} \lambda_i \cos^2(\theta_{\omega,i}), \tag{2.11}$$

depends strongly on how the vorticity vector aligns in the strain-rate eigenframe, figure 3. Here, $\theta_{\omega,i}$ is the angle between the vorticity and the ith eigenvector of the strain-rate tensor. The local enstrophy, and hence the velocity gradient magnitude, is increased when the vorticity vector aligns more with eigenvectors having positive (extensional) eigenvalues. Velocity gradient production rate via strain self-amplification is,

$$P_s = -3\lambda_1\lambda_2\lambda_3. \tag{2.12}$$

The strain rate amplifies itself when $\lambda_2 > 0$ but self-attenuates when $\lambda_2 < 0$, see figure 3. It is no surprise, then, that restricted Euler solutions tend toward a state with two positive strain-rate eigenvalues, $\lambda_1 = \lambda_2 = -\frac{1}{2}\lambda_3$, as they approach the finite-time singularity. Furthermore, the vorticity aligns with the eigenvector associated with the intermediate eigenvalue, λ_2, in this approach to singularity. Thus, both strain self-amplification and vorticity stretching together drive the finite-time singularity in restricted Euler.

Incompressible Navier–Stokes dynamics, with the non-local pressure Hessian and viscous term reintroduced, do not exhibit the finite-time singularity seen for the restricted Euler equation. Instead, there is a balance between vorticity and strain-rate as already discussed with (2.5). Betchov (1956) provided another relation for incompressible

homogeneous turbulence, namely,

$$-\langle S_{ij}S_{jk}S_{ki}\rangle = \tfrac{3}{4}\langle \omega_i S_{ij}\omega_j\rangle \quad \text{or} \quad \langle P_s\rangle = 3\langle P_\omega\rangle, \tag{2.13a,b}$$

which means that the average value of R (the third invariant of the velocity gradient tensor) is also zero, as enforced by the pressure via the constraint $\boldsymbol{\nabla}\cdot\boldsymbol{u}=0$. As with (2.5), (2.13*a*,*b*) is approximately true for high Reynolds number inhomogeneous flows. What this means is that, while the pressure enforces $\boldsymbol{\nabla}\cdot\boldsymbol{u}=0$ leading to an equal partition between dissipation and enstrophy, it also causes the strain-rate self-amplification to produce stronger velocity gradients at three times the rate of vorticity stretching.

The significance of the restricted Euler equation is that its signature features are unmistakably observed in the statistics of experiments and DNSs of the Navier–Stokes equations. Indeed, turbulent flows show a tendency of the vorticity to align with the strain-rate eigenvector associated with the intermediate eigenvalue, λ_2, which tends to be positive much more often than it is negative (Ashurst *et al.* 1987; Kerr 1987; Tsinober, Kit & Dracos 1992; Lund & Rogers 1994; Mullin & Dahm 2006; Gulitski *et al.* 2007). In addition, turbulence is characterized by enhanced probabilities of strong velocity gradients along the Vieillefosse manifold, $4Q^3+27R^2=0$ in the fourth quadrant, which is an attracting manifold along which the finite-time singularity occurs for restricted Euler (Cantwell 1993; Soria *et al.* 1994; Chong *et al.* 1998; Nomura & Post 1998; Ooi *et al.* 1999; Gulitski *et al.* 2007; Elsinga & Marusic 2010). While the non-local part of the pressure Hessian tensor, along with viscous effects, are important for describing turbulence quantitatively, many of the unique qualitative features of turbulent velocity gradients can be connected to restricted Euler dynamics.

In summary, velocity gradients in a fluid undergoing nonlinear self-advection ($\boldsymbol{u}\cdot\boldsymbol{\nabla u}$) naturally strengthen via vorticity stretching and strain self-amplification. Of these two dynamical processes, strain self-amplification is three times as strong on average, as enforced by the non-local action of the pressure. For more discussion about velocity gradient dynamics, as well as measurement and modelling, the reader is referred to (Tsinober 2009; Wallace 2009; Meneveau 2011). Next, the energy cascade is introduced using a spatial filtering formulation. As will be shown, this framework allows for directly relating the velocity gradient dynamics to the energy cascade.

2.4. *Spatial filtering and the energy cascade*

A spatial low-pass filter,

$$\bar{a}^\ell(\boldsymbol{x}) = \iiint_{-\infty}^{\infty} G_\ell(\boldsymbol{r})a(\boldsymbol{x}+\boldsymbol{r})\,\mathrm{d}\boldsymbol{r}, \quad \mathcal{F}\{\bar{a}^\ell\} = (2\pi)^3\mathcal{F}\{G_\ell\}\mathcal{F}\{\widehat{a}\} \tag{2.14a,b}$$

retains features of a field $a(\boldsymbol{x})$ that are larger than ℓ while removing features smaller than ℓ (Leonard 1975; Germano 1992). Here, $\mathcal{F}$ denotes the 3-D Fourier transform,

$$\mathcal{F}\{a\}(\boldsymbol{k}) = \frac{1}{(2\pi)^3}\iiint_{-\infty}^{\infty} a(\boldsymbol{x})\exp(-\mathrm{i}\boldsymbol{k}\cdot\boldsymbol{x})\,\mathrm{d}\boldsymbol{x}, \tag{2.15}$$

with inverse transform,

$$\mathcal{F}^{-1}\{b\}(\boldsymbol{x}) = \iiint_{-\infty}^{\infty} b(\boldsymbol{k})\exp(\mathrm{i}\boldsymbol{k}\cdot\boldsymbol{x})\,\mathrm{d}\boldsymbol{k}. \tag{2.16}$$

An example velocity field from the DNS of HIT is shown in figure 4, before and after the application of a spatial filter. The spatial filter may be interpreted as a form of local

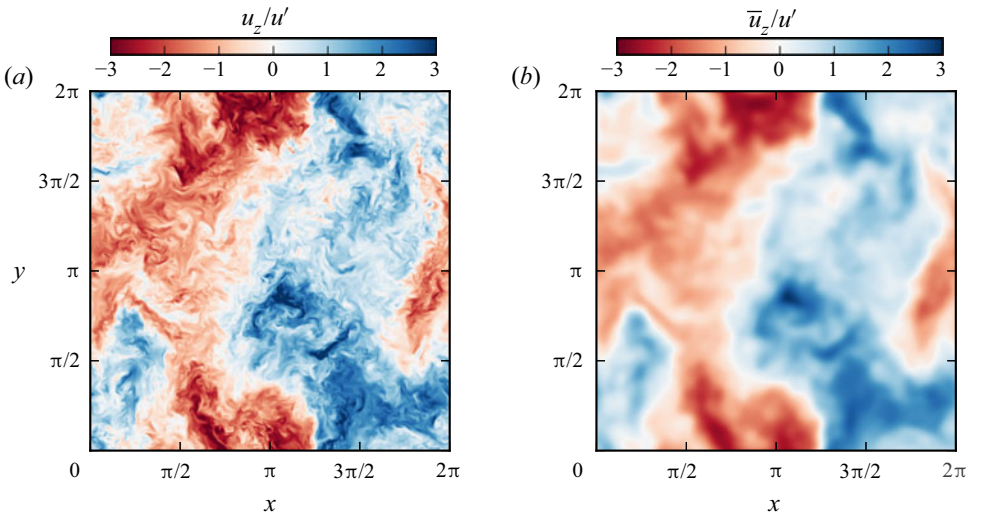

Figure 4. The fluid velocity in the z direction on an xy plane in the HIT simulation: (a) unfiltered, (b) filtered at $\ell = 25\eta$ using a Gaussian filter, (3.1a,b).

averaging, weighted by the filter kernel $G_\ell(\boldsymbol{r})$. Following Germano (1992), the generalized second moment is the difference of the filtered product and the product of two filtered fields,

$$\tau_\ell(a, b) = \overline{ab}^\ell - \bar{a}^\ell \bar{b}^\ell. \tag{2.17}$$

It is a generalized covariance of small-scale activity (smaller than ℓ).

The kinetic energy can be thus defined as the sum of large-scale and small-scale energies,

$$\tfrac{1}{2}\overline{u_i u_i}^\ell = \tfrac{1}{2}\bar{u}_i^\ell \bar{u}_i^\ell + \tfrac{1}{2}\tau_\ell(u_i, u_i). \tag{2.18}$$

If the filter kernel is positive semi-definite, i.e. $G_\ell(\boldsymbol{r}) \geq 0$ for all $\boldsymbol{r}$, then the subfilter-scale energy is positive everywhere, $\tau(u_i, u_i)(\boldsymbol{x}) \geq 0$ for all $\boldsymbol{x}$ (Vreman, Geurts & Kuerten 1994).

Applying a low-pass filter to the incompressible Navier–Stokes equations, (2.1a,b), results in an evolution equation for the filtered velocity field,

$$\frac{\partial \bar{u}_i^\ell}{\partial t} + \bar{u}_j^\ell \frac{\partial \bar{u}_i^\ell}{\partial x_j} = -\frac{\partial \bar{p}^\ell}{\partial x_i} + \nu \nabla^2 \bar{u}_i^\ell - \frac{\partial \tau_\ell(u_i, u_j)}{\partial x_j} + \bar{f}_i^\ell. \tag{2.19}$$

The main difference with the unfiltered Navier–Stokes equation (2.1a,b), is the introduction of the subfilter stress tensor's divergence on the right side. The dynamical equation for the large-scale kinetic energy directly follows from multiplication of (2.19) by $\bar{u}_i^\ell$,

$$\frac{\partial(\frac{1}{2}\bar{u}_i^\ell \bar{u}_i^\ell)}{\partial t} + \frac{\partial \Phi_j^\ell}{\partial x_j} = \bar{u}_i^\ell \bar{f}_i^\ell + \tau_\ell(u_i, u_j)\bar{S}_{ij}^\ell - 2\nu \bar{S}_{ij}^\ell \bar{S}_{ij}^\ell, \tag{2.20a}$$

where

$$\Phi_j^\ell = \tfrac{1}{2}\bar{u}_i^\ell \bar{u}_i^\ell \bar{u}_j^\ell + \bar{p}^\ell \bar{u}_j^\ell - 2\nu \bar{u}_i^\ell \bar{S}_{ij}^\ell + \bar{u}_i^\ell \tau_\ell(u_i, u_j). \tag{2.20b}$$

There are three source/sink terms. First, large-scale kinetic energy is produced though work done by the applied forcing function, $\bar{u}_i^\ell \bar{f}_i^\ell$. Second, the subfilter stress may add or

remove energy depending on its alignment with the filtered strain-rate tensor, $\tau_\ell(u_i, u_j)\bar{S}_{ij}^\ell$. Finally, the direct dissipation of large-scale kinetic energy by viscosity, $-2\nu\bar{S}_{ij}^\ell\bar{S}_{ij}^\ell$, is typically negligible if $\ell \gg \eta$.

An equation for total kinetic energy, $\frac{1}{2}\overline{u_i u_i}^\ell$, is constructed by multiplying (2.1*a*,*b*) by u_i and then filtering. Equation (2.20*a*) is subtracted from the resulting equation to form the transport equation for the small-scale energy,

$$\frac{\partial(\frac{1}{2}\tau_\ell(u_i, u_j))}{\partial t} + \frac{\partial \phi_j^\ell}{\partial x_j} = \tau_\ell(u_i, f_i) - \tau_\ell(u_i, u_j)\bar{S}_{ij}^\ell - 2\nu\tau_\ell(S_{ij}, S_{ij}), \tag{2.21a}$$

where

$$\phi_j^\ell = \tfrac{1}{2}\tau_\ell(u_i, u_i)\bar{u}_j^\ell + \tfrac{1}{2}\tau_\ell(u_i, u_i, u_j) + \tau_\ell(p, u_j) - 2\nu\tau_\ell(u_i, S_{ij}), \tag{2.21b}$$

where the second transport term is a generalized third moment (Germano 1992),

$$\tau_\ell(a, b, c) = \overline{abc}^\ell - \bar{a}^\ell\tau_\ell(b, c) - \bar{b}^\ell\tau_\ell(a, c) - \bar{c}^\ell\tau_\ell(a, b) - \bar{a}^\ell\bar{b}^\ell\bar{c}^\ell. \tag{2.22}$$

There are three sources/sinks in (2.21*a*), which have the following significance. The first source is direct forcing of the small scales, $\tau_\ell(u_i, f_i)$, which is typically negligible for $\ell \ll L$. The second is the same term, $-\tau_\ell(u_i, u_j)\bar{S}_{ij}^\ell$, as appears with opposite sign in the large-scale energy equation (2.20*a*). This term represents the rate at which energy is transferred from motions of size larger than ℓ to motions of size smaller than ℓ. Thus, the energy cascade rate is defined as (Leonard 1975; Germano 1992; Meneveau & Katz 2000),

$$\Pi^\ell = -\mathring{\tau}_\ell(u_i, u_j)\bar{S}_{ij}^\ell, \tag{2.23}$$

where the overset circle indicates the deviatoric component of the tensor,

$$\mathring{\tau}_\ell(u_i, u_j) = \tau_\ell(u_i, u_j) - \tfrac{1}{3}\tau_\ell(u_k, u_k)\delta_{ij}. \tag{2.24}$$

The isotropic part of the subfilter stress tensor does not contribute to the energy cascade rate, Π^ℓ, because the trace of $\bar{S}^\ell$ is zero due to incompressibility. Positive cascade rate indicates energy transfer from large to small scales and negative rate indicates backscatter or inverse cascade. It may be interpreted as the rate at which large-scale motions do work on small-scale motions (Ballouz & Ouellette 2018).

Averaging (2.20*a*) and (2.21*a*) for a stationary, homogeneous flow yields, respectively,

$$0 = \langle\bar{u}_i^\ell\bar{f}_i^\ell\rangle + \langle\tau_\ell(u_i, u_j)\bar{S}_{ij}^\ell\rangle - 2\nu\langle\bar{S}_{ij}^\ell\bar{S}_{ij}^\ell\rangle, \tag{2.25}$$

$$0 = \langle\tau_\ell(u_i, f_i)\rangle - \langle\tau_\ell(u_i, u_j)\bar{S}_{ij}^\ell\rangle - 2\nu\langle\tau_\ell(S_{ij}, S_{ij})\rangle. \tag{2.26}$$

In the inertial range of turbulence, $\eta \ll \ell \ll L$, the viscous dissipation of the large scales and forcing of the small scales may be neglected,

$$\langle u_i f_i\rangle \approx \langle\bar{u}_i^\ell\bar{f}_i^\ell\rangle \approx -\langle\tau_\ell(u_i, u_j)\bar{S}_{ij}^\ell\rangle \approx 2\nu\langle\tau_\ell(S_{ij}, S_{ij})\rangle \approx 2\nu\langle S_{ij}S_{ij}\rangle. \tag{2.27}$$

More simply, the inertial range is the range length scales, ℓ, for which $\langle\Pi\rangle \approx \langle\epsilon\rangle$. Figure 5(*a*) tests for scales where this relation approximately holds.

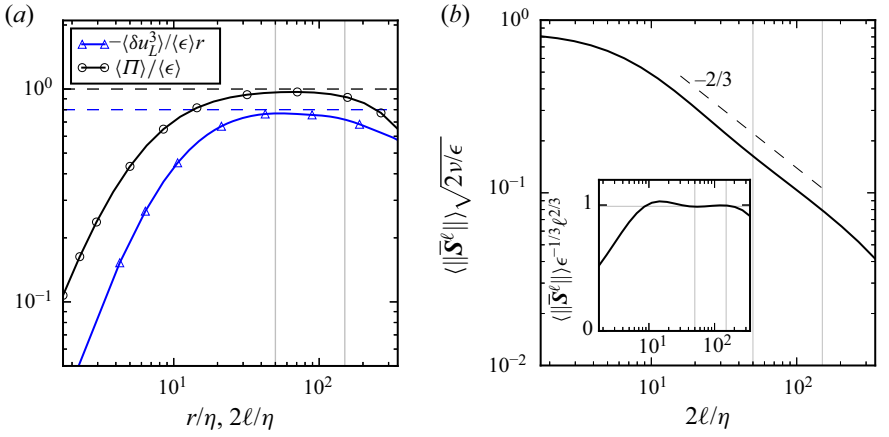

Figure 5. (*a*) The pre-multiplied third-order longitudinal structure function alongside the mean interscale energy transfer. (*b*) The average norm of the filtered strain-rate tensor as function of filter width, ℓ. A $-2/3$ power law is consistent with inertial range behaviour. The inset is premultiplied by $\ell^{2/3}$. In both panels, the two vertical grey lines are at $2\ell/\eta = 50$ and 150, indicating the approximate inertial range of scales. The integral length scale is $2L/\eta = 920$.

2.5. *Filtered velocity gradients*

Velocity increments,

$$\delta u_i(\boldsymbol{r}; \boldsymbol{x}) = u_i(\boldsymbol{x} + \boldsymbol{r}) - u_i(\boldsymbol{x}) \tag{2.28}$$

and structure functions are prominent tools of classical turbulence theory. Filtered velocity gradients are intimately related to velocity increments (Eyink 1995),

$$\bar{A}_{ij}^\ell(\boldsymbol{x}) \equiv \frac{\partial \bar{u}_i}{\partial x_j}(\boldsymbol{x}) = \iiint \mathrm{d}\boldsymbol{r}\, \frac{\partial G}{\partial r_j}\bigg|_{\boldsymbol{r}} \delta u_i(\boldsymbol{r}, \boldsymbol{x}) = \int_0^\infty \mathrm{d}\rho \frac{\mathrm{d}G}{\mathrm{d}\rho} \left[\oiint \mathrm{d}S \frac{r_j}{|\boldsymbol{r}|} \delta u_i(\boldsymbol{r}; \boldsymbol{x}) \right], \tag{2.29}$$

where the filter kernel is assumed to be spherically symmetric. That is, the filtered velocity gradient is an averaging of velocity increments weighted by the gradient of the filter kernel. Thus, filtered velocity gradients contain information about velocity increments in the flow, arranged so as to illuminate the local topology of the flow at scale ℓ. Filtered velocity gradients can be decomposed into rotation and deformation at scale ℓ,

$$\bar{A}_{ij}^\ell = \bar{S}_{ij}^\ell + \bar{\Omega}_{ij}^\ell, \quad \bar{S}_{ij}^\ell = \tfrac{1}{2}(\bar{A}_{ij}^\ell + \bar{A}_{ji}^\ell), \quad \bar{\Omega}_{ij}^\ell = \tfrac{1}{2}(\bar{A}_{ij}^\ell - \bar{A}_{ji}^\ell), \tag{2.30a–c}$$

$$\bar{\Omega}_{ij}^\ell = -\tfrac{1}{2}\epsilon_{ijk}\bar{\omega}_k^\ell, \quad \bar{\omega}_i^\ell = -\epsilon_{ijk}\bar{\Omega}_{jk}^\ell, \tag{2.31a,b}$$

$$\tfrac{1}{2}\|\bar{\boldsymbol{A}}^\ell\|^2 = \tfrac{1}{4}|\bar{\boldsymbol{\omega}}^\ell|^2 + \tfrac{1}{2}\|\bar{\boldsymbol{S}}^\ell\|^2, \quad \langle \|\bar{\boldsymbol{S}}^\ell\|^2 \rangle = \tfrac{1}{2}\langle |\bar{\boldsymbol{\omega}}^\ell|^2 \rangle. \tag{2.32a,b}$$

The K41 scaling of the filtered strain-rate norm, $\|\bar{\boldsymbol{S}}^\ell\| \sim \ell^{-2/3}$, is shown in figure 5(*b*) as another indication of what filter widths may be considered to be in the inertial range.

Figure 6 shows vorticity and filtered vorticity fields from the same snapshot used for figure 4. It is evident that the vorticity is predominantly organized at the smallest scales of motion, near η. This is true of the velocity gradient tensor in general. However, the filtered velocity gradient, as demonstrated for the filtered vorticity, is primarily organized at a scale near the filter width. Thus, the filtered velocity gradient provides a good definition of fluid motions at scale ℓ. Comparing figures 4 and 6, note the striking visual difference in how filtering effects the velocity field and the velocity gradient field.

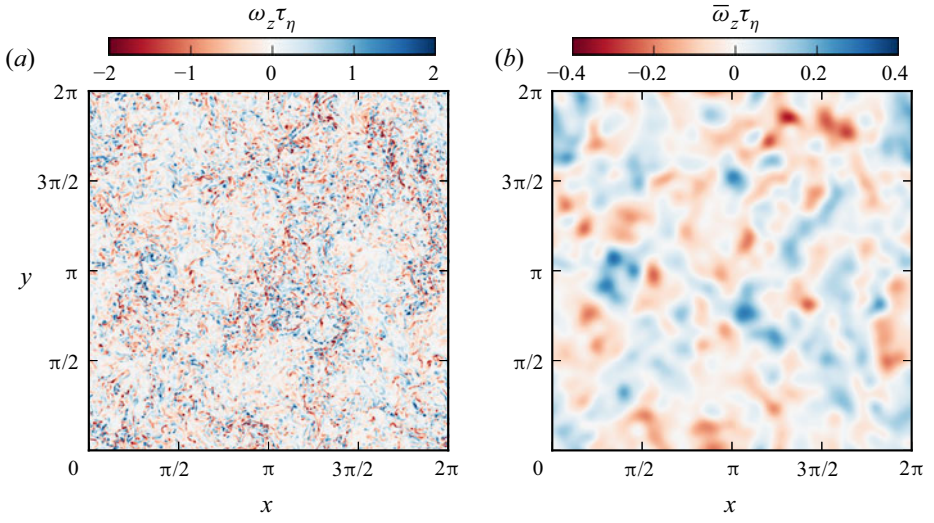

Figure 6. The z component of vorticity along the same xy plane from figure 4: (a) unfiltered, (b) filtered at $\ell = 25\eta$ using a Gaussian filter, (3.1a,b).

Like the filtered velocity gradient, the subfilter stress tensor may also be written as a local averaging of velocity increments (Constantin, E & Titi 1994; Eyink 1995),

$$\tau_\ell(u_i, u_j) = \left[\iiint \mathrm{d}\boldsymbol{r} G_\ell(\boldsymbol{r})\delta u_i(\boldsymbol{r};\boldsymbol{x})\delta u_j(\boldsymbol{r};\boldsymbol{x})\right] - \left[\iiint \mathrm{d}\boldsymbol{r} G_\ell(\boldsymbol{r})\delta u_i(\boldsymbol{r};\boldsymbol{x})\right]\left[\iiint \mathrm{d}\boldsymbol{r} G_\ell(\boldsymbol{r})\delta u_j(\boldsymbol{r};\boldsymbol{x})\right]. \tag{2.33}$$

In this way, it can be directly shown that

$$\tau_\ell(u_i, u_j) \sim \delta u^2 \quad \text{and} \quad \bar{S}^\ell_{ij} \sim \delta u/\ell, \quad \text{therefore } \Pi^\ell \sim \delta u^3/\ell, \tag{2.34a,b}$$

so that the inertial range equation, from (2.27), in the form $\langle \Pi^\ell \rangle = \langle \epsilon \rangle$ is in some ways analogous to the celebrated four-fifths law of Kolmogorov (1941a), i.e. $\langle \delta u_L^3(r) \rangle = -\frac{4}{5}\langle \epsilon \rangle r$. The similarity between these two is highlighted in figure 5(a), which includes the pre-multiplied third-order longitudinal structure function alongside $\langle \Pi \rangle / \langle \epsilon \rangle$. These two are similar diagnostics of inertial range scales.

2.6. *Filtered velocity gradient dynamics*

Definitively linking the energy cascade rate with vorticity stretching and strain self-amplification is naturally done by considering the dynamics of filtered velocity gradients. Viewing the filtered flow as the collection of fluid particles of size $\sim \ell$ following trajectories set by $\bar{\boldsymbol{u}}^\ell$, each particle's rotation and deformation dynamics may be described by the gradient of filtered Navier–Stokes, (2.19), which reads

$$\frac{\bar{\mathrm{D}}\bar{A}^\ell_{ij}}{\bar{\mathrm{D}}t} = \underbrace{-\left(\bar{A}^\ell_{ik}\bar{A}^\ell_{kj} - \frac{1}{3}\bar{A}^\ell_{mn}\bar{A}^\ell_{nm}\delta_{ij}\right)}_{\textit{autonomous dynamics}} - \left(\frac{\partial^2 \bar{p}^\ell}{\partial x_i x_j} - \frac{1}{3}\nabla^2\bar{p}^\ell\delta_{ij}\right) + \nu\nabla^2\bar{A}^\ell_{ij} - \frac{\partial \tau_\ell(u_i, u_k)}{\partial x_j \partial x_k}. \tag{2.35}$$

This equation gives the dynamical evolution of filtered velocity gradients along filtered Lagrangian trajectories, $\overline{\mathrm{D}}/\overline{\mathrm{D}t} = \partial/\partial t + \bar{\boldsymbol{u}}^{\ell} \cdot \boldsymbol{\nabla}$. The difference from unfiltered velocity gradients, (2.8), is the gradient of the subfilter scale force. The dynamical consequence of the subfilter-scale force is subtle, and the restricted Euler-like features observed for unfiltered velocity gradients are also seen for filtered ones (Danish & Meneveau 2018). In other words, the autonomous dynamics of filtered velocity gradients is very influential in setting statistical trends in turbulent flows, as previously seen for unfiltered gradients.

The restricted Euler equation for filtered velocity gradient dynamics again results by neglecting all except the autonomous terms in (2.35),

$$\frac{\mathrm{D}}{\mathrm{D}t}\left(\frac{1}{2}\|\bar{\boldsymbol{A}}^{\ell}\|^2\right) = P_{\bar{\omega}} + P_{\bar{s}} = \frac{1}{4}\bar{\omega}_i^{\ell}\bar{S}_{ij}^{\ell}\bar{\omega}_j^{\ell} - \bar{S}_{ij}^{\ell}\bar{S}_{jk}^{\ell}\bar{S}_{ki}^{\ell}. \tag{2.36}$$

This, which now neglects interactions with both nearby particles and subfilter scales, highlights the role of vorticity stretching and strain self-amplification in increasing the magnitude of filtered velocity gradients. Recall from (2.32*a*,*b*) that the filtered vorticity and strain-rate are also held in statistical equi-partition by the zero divergence condition, $\boldsymbol{\nabla} \cdot \bar{\boldsymbol{u}}^{\ell} = 0$, owing to the filtered pressure. In addition, the average amount of strain self-amplification is also held at three times the vorticity stretching for filtered fields,

$$-\langle \bar{S}_{ij}^{\ell}\bar{S}_{jk}^{\ell}\bar{S}_{ki}^{\ell}\rangle = \tfrac{3}{4}\langle \bar{\omega}_i^{\ell}\bar{S}_{ij}^{\ell}\bar{\omega}_j^{\ell}\rangle \quad \text{or} \quad \langle P_{\bar{s}}\rangle = 3\langle P_{\bar{\omega}}\rangle. \tag{2.37a,b}$$

Equation (2.36) is only meant to demonstrate the relationship of $P_{\bar{s}}$ and $P_{\bar{\omega}}$ with the growth of filtered velocity gradients. For a full description of real turbulent flows, the pressure, viscous, and subfilter terms must be retained.

3. Energy cascade in terms of filtered velocity gradients

3.1. *Theory*

The local energy cascade rate, $\Pi(\boldsymbol{x}, t)$, is determined by the filtered strain-rate tensor, the subfilter stress tensor and how those two align. Johnson (2020*a*) demonstrated how the subfilter stress tensor may be phrased in terms of filtered velocity gradients across all scales $\leq \ell$, so that the energy cascade rate may be written solely in terms of filtered velocity gradients. This result directly connects the restricted Euler singularity with the fact that turbulence generates a net cascade from large to small scales. A summary of the derivation is presented below, with more details provided in Appendix C.

A Gaussian filter kernel

$$G_{\ell}(\boldsymbol{r}) = \mathcal{N}\exp\left(-\frac{|\boldsymbol{r}|^2}{2\ell^2}\right), \quad (2\pi)^3\mathcal{F}\{G_{\ell}\}(\boldsymbol{k}) = \exp\left(-\frac{1}{2}|\boldsymbol{k}|^2\ell^2\right), \tag{3.1a,b}$$

decays rapidly in both physical space and wavenumber space, and is thus a popular choice for studies involving explicit filters (Borue & Orszag 1998; Domaradzki & Carati 2007*b*; Eyink & Aluie 2009; Leung, Swaminathan & Davidson 2012; Cardesa *et al.* 2015; Lozano-Durán *et al.* 2016; Buzzicotti *et al.* 2018; Alexakis & Chibbaro 2020; Dong *et al.* 2020; Portwood *et al.* 2020; Vela-Martín & Jiménez 2021). Here, the definition of the filter width, ℓ, is chosen such that its gradient, $\mathrm{d}G/\mathrm{d}r$, is maximum at $r = \ell$. That is, velocity increments at separation $r = \ell$ have are the most heavily weighted when constructing the filtered velocity gradient according to (2.29). Note that in figure 5(*a*), 2ℓ appears to correspond to the structure function separation r. This happens because, in (2.29), the velocity increments with equal and opposite separation vectors of length ℓ are essentially

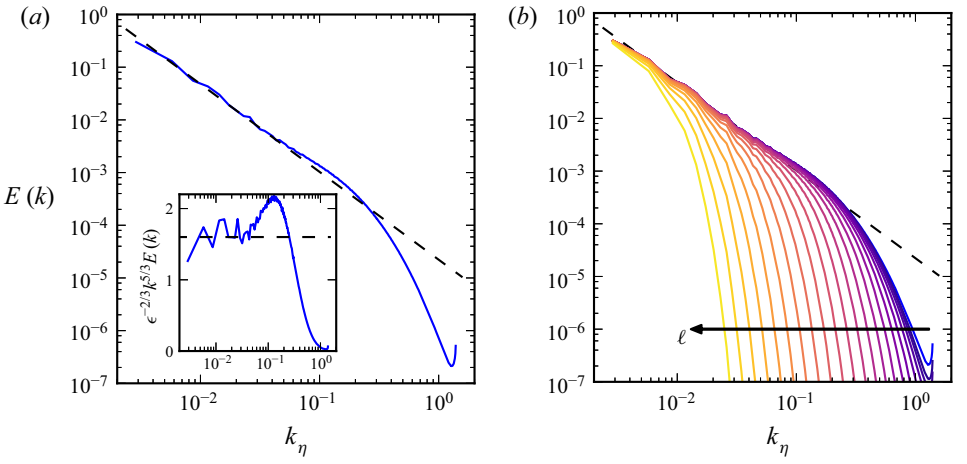

Figure 7. (*a*) Average energy spectrum from the HIT simulation, and (*b*) filtered spectra using a Gaussian filter with various values of $0.9\eta \leq \ell \leq 170\eta$ spaced evenly in logarithmic space. The black dashed line indicates the inertial range spectrum, $E(k) = 1.6\epsilon^{2/3}k^{-5/3}$. The inset in panel (*a*) shows the premultiplied spectrum on a log–linear plot.

combined to form velocity increments at 2ℓ, which are integrated on a half-sphere to form the filtered velocity gradient.

The Gaussian filter has already been demonstrated in physical space in figures 4 and 6. Figure 7 shows average energy spectra with and without a Gaussian filter. Note that the unfiltered spectrum decays as a (stretched) exponential in the dissipation range (Townsend 1951; Kraichnan 1959; Novikov 1961; Qian 1984; Sreenivasan 1985; Foias, Manley & Sirovich 1990; Smith & Reynolds 1991; Manley 1992; Sanada 1992; Chen *et al.* 1993; Saddoughi & Veeravalli 1994; Sirovich, Smith & Yakhot 1994; Ishihara *et al.* 2005; Khurshid, Donzis & Sreenivasan 2018; Buaria & Sreenivasan 2020), and the effect of the Gaussian filter moves this exponential-like decay to lower wavenumbers. The unfiltered spectrum shows agreement with the standard Kolmogorov spectrum, $E(k) = 1.6\epsilon^{2/3}k^{-5/3}$ over a limited range of wavenumbers $k\eta \ll 1$. A 'spectral bump', as typically observed, is evident near $0.1 < k\eta < 0.2$ (Qian 1984; Falkovich 1994; Lohse & Müller-Groeling 1995; Kurien, Taylor & Matsumoto 2004; Bershadskii 2008; Frisch *et al.* 2008; Meyers & Meneveau 2008; Mininni *et al.* 2008; Donzis & Sreenivasan 2010). This is usually associated with a 'bottleneck effect' at the end of the cascade in which viscosity is slightly too slow in dissipating energy as it arrives from larger scales, resulting in a slight pile-up of energy. While the filtering approach does smooth out this effect to some degree, it is visible for the filtered strain-rate norm in the inset of figure 5(*b*) in the range $5 < \ell/\eta < 10$.

Because the Gaussian kernel serves as the Green's function for the diffusion equation, a filtered quantity is the solution to

$$\frac{\partial \bar{a}^\ell}{\partial(\ell^2)} = \frac{1}{2}\nabla^2 \bar{a}^\ell, \quad \text{with initial condition } \bar{a}^{\ell=0}(\boldsymbol{x}) = a(\boldsymbol{x}), \tag{3.2}$$

where the square of the filter width, ℓ^2, serves as a time-like variable. The initial condition at $\ell = 0$ is the unfiltered field. From this observation, it is straightforward to show that any generalized second moment may be written as

$$\frac{\partial \tau_\ell(a,b)}{\partial(\ell^2)} = \frac{1}{2}\nabla^2 \tau_\ell(a,b) + \frac{\partial \bar{a}^\ell}{\partial x_k}\frac{\partial \bar{b}^\ell}{\partial x_k}, \quad \text{with initial condition } \tau_{\ell=0}(a,b) = 0. \tag{3.3}$$

Thus, the generalized second moment is the solution to a forced diffusion equation with zero initial condition. The forcing is the product of filtered gradients as a function of scale (the time-like variable). The formal solution for this forced diffusion equation is

$$\tau_\ell(a,b) = \int_0^{\ell^2} \mathrm{d}\alpha \, \overline{\overline{\frac{\partial a}{\partial x_k}}^{\sqrt{\alpha}} \overline{\frac{\partial b}{\partial x_k}}^{\sqrt{\alpha}}}^{\beta}, \tag{3.4}$$

where $\beta \equiv \sqrt{\ell^2 - \alpha}$ is the conjugate filter such that successively filtering at $\sqrt{\alpha}$ and β is equivalent to applying a single filter at scale ℓ,

$$\overline{\bar{a}^{\sqrt{\alpha}}}^{\beta} = \bar{a}^{\ell}. \tag{3.5}$$

The formal solution in (3.3) contains two components,

$$\tau_\ell(a,b) = \ell^2 \overline{\frac{\partial a}{\partial x_i}}^{\ell} \overline{\frac{\partial b}{\partial x_i}}^{\ell} + \int_0^{\ell^2} \mathrm{d}\alpha \, \tau_\beta \left(\overline{\frac{\partial a}{\partial x_k}}^{\sqrt{\alpha}}, \overline{\frac{\partial b}{\partial x_k}}^{\sqrt{\alpha}} \right). \tag{3.6}$$

The first component is the product of gradients at the filter scale ℓ and the second component involves subfilter-scale generalized second moments of gradients filtered at scales smaller than ℓ. Equation (3.6) is applied to the subfilter stress, $\tau_\ell(u_i, u_j)$, by setting $a = u_i$ and $b = u_j$. Contracting with $\bar{S}_{ij}^{\ell}$ to compute the energy cascade rate, Π^{ℓ}, results in

$$\Pi^{\ell} = \Pi_{s1}^{\ell} + \Pi_{\omega 1}^{\ell} + \Pi_{s2}^{\ell} + \Pi_{\omega 2}^{\ell} + \Pi_{c}^{\ell}. \tag{3.7}$$

The five components of (3.7) are defined and interpreted as follows.

The first two terms involve velocity gradients filtered at scale ℓ only. First, the self-amplification of the strain rate at scale ℓ transfers energy across scale ℓ at a rate,

$$\Pi_{s1}^{\ell} = \ell^2 P_{\bar{s}} = -\ell^2 \bar{S}_{ij}^{\ell} \bar{S}_{jk}^{\ell} \bar{S}_{ki}^{\ell} = -3\ell^2 \lambda_1^{\ell} \lambda_2^{\ell} \lambda_3^{\ell}, \tag{3.8}$$

where λ_i^{ℓ} are the 3 eigenvalues of the strain-rate tensor filtered at scale ℓ. This term gives mathematical definition to the simplified process sketched in figure 2. The strain-rate triple product represents the production of larger strain rates with smaller spatial extent which may be thought of as similar to the dynamics of the Burgers equation. The drawing in figure 2 is meant only to provide a useful intuitive feel for how Π_{s1}^{ℓ} transfers energy to smaller scales, not a sweeping claim that all regions with high Π_{s1} resemble the simplified sketch.

Similarly, the vorticity at scale ℓ is stretched by the strain rate at the same scale, which transfers energy

$$\Pi_{\omega 1}^{\ell} = \ell^2 P_{\bar{\omega}} = \frac{1}{4}\ell^2 \bar{S}_{ij}^{\ell} \bar{\omega}_i^{\ell} \bar{\omega}_j^{\ell} = \frac{1}{4}\ell^2 \left| \bar{\boldsymbol{\omega}}^{\ell} \right|^2 \sum_{i=1}^{3} \lambda_i^{\ell} \cos^2(\theta_{\omega,i}^{\ell}), \tag{3.9}$$

where $\theta_{\omega,i}^{\ell}$ are the angles between each corresponding eigenvector and the vorticity vector filtered at scale ℓ. As such, this term quantifies the local rate at which vortex stretching, as sketched in a simplified manner in figure 1, passes energy across scale ℓ.

For these first two terms, a subscript '1' is used to denote that these rates involve quantities at a single filter scale. In fact, these two terms appear both in (3.7) and in the velocity gradient evolution, (2.36). The same processes responsible for increasing

the filtered velocity gradient magnitude also redistribute energy to sub-filter scales, thus connecting the restricted Euler singularity with the energy cascade. It is also possible to obtain these two as leading-order terms in an infinite expansion in at least two ways.

First, using spatial filtering with a more general filter shape, the Taylor expansion of the Leonard stress is led by these two terms (Pope 2000). Truncation of this expansion is sometimes called the Clark model, or tensor diffusivity model (Clark, Ferziger & Reynolds 1979; Borue & Orszag 1998). This model performs well in *a priori* tests, but does not remove large-scale energy at a sufficient rate when used with LES (Vreman, Geurts & Kuerten 1996, 1997). Intriguingly, it may be shown that the Lagrangian memory effects in the evolution of the subfilter stress tensor are correctly mimicked by the tensor diffusivity model (Johnson 2020*b*). In practice, the tensor diffusivity model is often supplemented with an eddy viscosity model (Clark *et al.* 1979; Vreman *et al.* 1996, 1997). Eyink (2006) extended this result to a multiscale gradient expansion for the full subfilter stress tensor, but still relied on truncating infinite series. Carbone & Bragg (2020) provided an alternative derivation of single-scale vorticity stretching and strain self-amplification as leading-order terms in an infinite series. In that case, the Kármán–Howarth–Monin equation (de Kármán & Howarth 1938; Monin & Yaglom 1975; Hill 2001) is used with filtered velocity gradients substituted as the leading-order term in the evaluation of velocity increments. Importantly, the result highlights agreement between velocity increment and filtering approaches to the energy cascade, indicating a degree of objectivity to this result (see, e.g. objections in Tsinober 2009).

The true advantage of the result from Johnson (2020*a*), (3.7), lies in the remaining three terms. These cascade rates involve interactions between the strain rate filtered at scale ℓ and velocity gradients at scales smaller than ℓ. They are given a subscript '2' to denote their multiscale nature (specifically, the sum of interactions involving two different scales). First, the cascade rate due to the amplification of small-scale strain by larger-scale strain is

$$\Pi^{\ell}_{s2} = -\bar{S}^{\ell}_{ij}\int_0^{\ell^2} \mathrm{d}\alpha\, \tau_\beta(\bar{S}^{\sqrt{\alpha}}_{jk}, \bar{S}^{\sqrt{\alpha}}_{ki}) = -\int_0^{\ell^2} \mathrm{d}\alpha\, \bar{S}^{\ell}_{ij}\tau_\beta(\bar{S}^{\sqrt{\alpha}}_{jk}, \bar{S}^{\sqrt{\alpha}}_{ki}). \tag{3.10}$$

For this term, $\bar{\boldsymbol{S}}^{\ell}$ represents the strain rate at the filter scale where the cascade rate is evaluated and the generalized second moment of $\bar{\boldsymbol{S}}^{\sqrt{\alpha}}$ in the integral represents smaller-scale strain rates being amplified as energy is passed down the cascade. This process may be thought of as a multiscale generalization of figure 2. Thus, $\bar{\boldsymbol{S}}^{\ell}$ amplifies strain rates at all scales $\sqrt{\alpha} < \ell$ and the resulting energy cascade rate is constructed by integrating over all smaller scales.

Similarly, the stretching of small-scale vorticity by larger-scale strain is

$$\Pi^{\ell}_{\omega 2} = \bar{S}^{\ell}_{ij}\int_0^{\ell^2} \mathrm{d}\alpha\, \tau_\beta(\bar{\omega}^{\sqrt{\alpha}}_{i}, \bar{\omega}^{\sqrt{\alpha}}_{j}) = \int_0^{\ell^2} \mathrm{d}\alpha\, \bar{S}^{\ell}_{ij}\tau_\beta(\bar{\omega}^{\sqrt{\alpha}}_{i}, \bar{\omega}^{\sqrt{\alpha}}_{j}). \tag{3.11}$$

In this mechanism, the enstrophy at scales $\sqrt{\alpha} < \ell$ is amplified as it aligns with extensional strain rates, $\boldsymbol{S}^{\ell}$, organized at larger scales, figure 1. This results in an energy cascade rate across scale ℓ.

Finally, the last term in (3.7) represents the contribution to the energy cascade rate from larger-scale strain rates acting on smaller-scale strain–vorticity covariance,

$$\Pi^{\ell}_{c} = \Pi^{\ell}_{c2} = \bar{S}^{\ell}_{ij}\int_0^{\ell^2} \mathrm{d}\alpha[\tau_\beta(\bar{S}^{\sqrt{\alpha}}_{jk}, \bar{\Omega}^{\sqrt{\alpha}}_{ki}) - \tau_\beta(\bar{\Omega}^{\sqrt{\alpha}}_{jk}, \bar{S}^{\sqrt{\alpha}}_{ki})]. \tag{3.12}$$

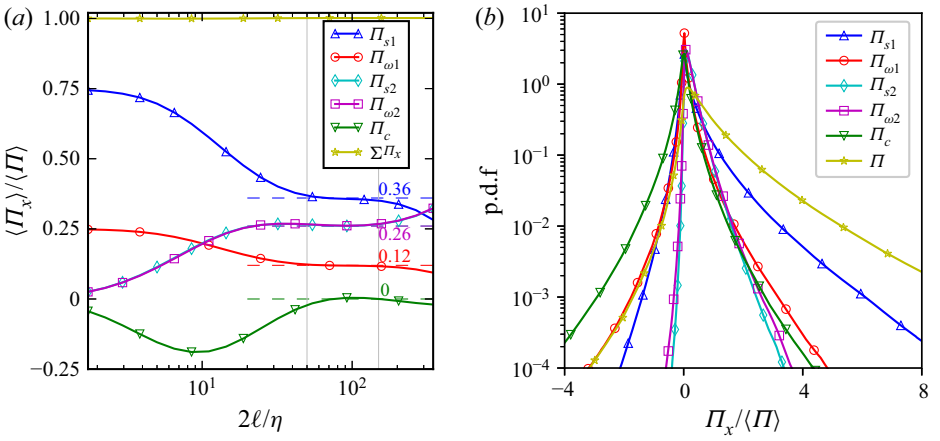

Figure 8. (*a*) The mean contribution of each cascade mechanism as a function of filter width. (*b*) The probability density functions of each component of the energy cascade rate from (3.7) at $\ell = 46\eta$. The two vertical grey lines are at $2\ell/\eta = 50$ and 150, indicating the approximate inertial range of scales. The integral length scale is at $2L/\eta = 920$.

In this final term, the strain rate at scale ℓ amplifies or attenuates the generalized subfilter covariance of strain rate and vorticity at all scales $\sqrt{\alpha} < \ell$. This term is given the subscript 'c', denoting it as a cross-term between both strain rate and vorticity. It is the only of the five terms not interpretable as vorticity stretching of strain self-amplification. Its meaning is less obvious, but one potential interpretation is given in § 3.3 while considering the inverse energy cascade in two dimensions.

3.2. *Results*

Figure 8(*a*) shows the net contribution of each dynamical mechanism to the cascade rate, as a fraction of the total cascade rate, which is shown figure 5(*a*). First, the sum of all five contributions is equal to unity, confirming the correctness of (3.7) in a spatially averaged sense. The point-wise accuracy of (3.7) is also confirmed in Appendix A, which also includes a brief study of its accuracy when some terms are neglected.

In the dissipative range, $\ell \sim \eta$, the three multiscale terms are small and the two single-scale terms comprise the cascade at the specified ratio of 3:1. In the range of filter widths previously identified as the inertial range, $25 < \ell/\eta < 75$ for this simulation, the fractional contribution of each cascade rate is constant, indicating some degree of self-similarity. Each plateau is fitted to two decimal places as reported in the figure. Note that $\langle \Pi_c \rangle \approx 0$ so that the other four terms are responsible for establishing the cascade rate.

In the inertial range, the sum of the two single-scale rates account for approximately half of the full cascade rate, with their multiscale analogues accounting for the other half. The amplification of strain rates, both single-scale and multiscale, account for roughly 5/8 of the energy cascade rate, with the remaining 3/8 due to vorticity stretching. Interestingly, the strain–vorticity covariance term supplies a negative cascade rate at filter widths corresponding to the spectral bump, offering a potential clue to the dynamical causes of the bottleneck effect. Also, the averages of Π_{s2} and $\Pi_{\omega 2}$ are indistinguishable in figure 8(*a*). At first glance, it seems there could exist some precise relationship between the two. However, the author was not able to identify any such analytical relationship, and inspection of the

numerical values plotted in figure 8(*a*) suggested that these terms were very close but not exactly equal.

The probability density functions (PDFs) of each contribution to the energy cascade rate from (3.7) are shown in figure 8(*b*) with filter width in the middle of the inertial range. The total cascade rate PDF is strongly skewed with relatively rare backscatter events. The net backscatter is less than 2 % of the total average cascade rate. The single-scale strain self-amplification, Π_{s1}, is also strongly skewed and has the most probable extreme positive events of any of the five components. The single-scale vorticity stretching, $\Pi_{\omega 1}$ is much less skewed toward downscale energy cascade. The multiscale strain amplification and vorticity stretching, Π_{s2} and $\Pi_{\omega 2}$, are extremely skewed and almost never negative. Finally, the amplification of subfilter strain–vorticity covariance, Π_c, is relatively symmetric and has the most probable extreme negative events. The PDFs of the energy cascade rates are explored as a function of filter width in Appendix B.

3.3. *Implications for the inverse cascade in 2-D turbulence*

The main topic of this paper is the energy cascade in 3-D flows. However, it is worthwhile to comment on implications for the inverse cascade of energy in two dimensions. Of the five terms on the right side of (3.7), only the fifth term is non-zero. All vorticity stretching and strain amplification terms vanish exactly in 2-D incompressible flows. Thus

$$\Pi^\ell = \Pi^\ell_{c2} = \bar{S}^\ell_{ij} \int_0^{\ell^2} \mathrm{d}\alpha [\tau_\beta(\bar{S}^{\sqrt{\alpha}}_{jk}, \bar{\Omega}^{\sqrt{\alpha}}_{ki}) - \tau_\beta(\bar{\Omega}^{\sqrt{\alpha}}_{jk}, \bar{S}^{\sqrt{\alpha}}_{ki})]. \tag{3.13}$$

Taking the eigenframe of the strain rate at scale ℓ,

$$\Pi^\ell(\boldsymbol{x}) = 2 \int_0^{\ell^2} \mathrm{d}\alpha \iiint \mathrm{d}\boldsymbol{r} G_\beta(\boldsymbol{r}) \lambda^\ell(\boldsymbol{x}) \lambda^{\sqrt{\alpha}}(\boldsymbol{x}+\boldsymbol{r}) \bar{\omega}^{\sqrt{\alpha}}(\boldsymbol{x}+\boldsymbol{r}) \sin 2\phi(\boldsymbol{x}, \boldsymbol{r}), \tag{3.14}$$

where $\phi(\boldsymbol{x}, \boldsymbol{r})$ is the angle of the eigenvectors of $\bar{\boldsymbol{S}}^{\sqrt{\alpha}}(\boldsymbol{x}+\boldsymbol{r})$ with respect to the eigenvectors of $\bar{\boldsymbol{S}}^\ell(\boldsymbol{x})$. Here, the eigenvalues of the strain rate are λ and $-\lambda$. If the strain-rate eigenvectors at ℓ and $\sqrt{\alpha}$ align parallel or perpendicular, then there is no transfer of energy. Maximum transfer of energy across scale ℓ occurs for $\pm 45^\mathrm{o}$, with the direction of the transfer also depending on the sign of vorticity. An inverse cascade is supported when smaller-scale strain rate is misaligned with larger-scale strain rate in the opposite rotational direction as the vorticity.

One such (cartoon-ish) scenario is sketched in figure 9. As a clockwise vortex ($\omega < 0$) is subjected to a larger-scale strain rate, it is flattened or thinned into a shear layer with strain-rate eigenvalues at 45° from the larger-scale strain. The resulting alignment produces a maximum inverse cascade rate. This is the vortex thinning mechanism of the 2-D inverse cascade (Kraichnan 1976; Chen *et al.* 2006; Xiao *et al.* 2009).

Therefore, (3.7) represents a comprehensive view of interscale energy transfer in two- and 3-D turbulence. It is interesting to note (G.L. Eyink, private communication) that this approach may be thought of as a sort of differential renormalization group analysis (Eyink 2018). While vorticity stretching and (to some degree) strain self-amplification are commonly discussed as cascade mechanisms in 3-D turbulence, it should not be a surprise that the vortex thinning mechanism posited for the 2-D inverse cascade is at least a possible mechanism for energy transfer in three dimensions as well. Thus, while (3.7) from Johnson (2020*a*) clearly identifies the roles of vorticity stretching and strain

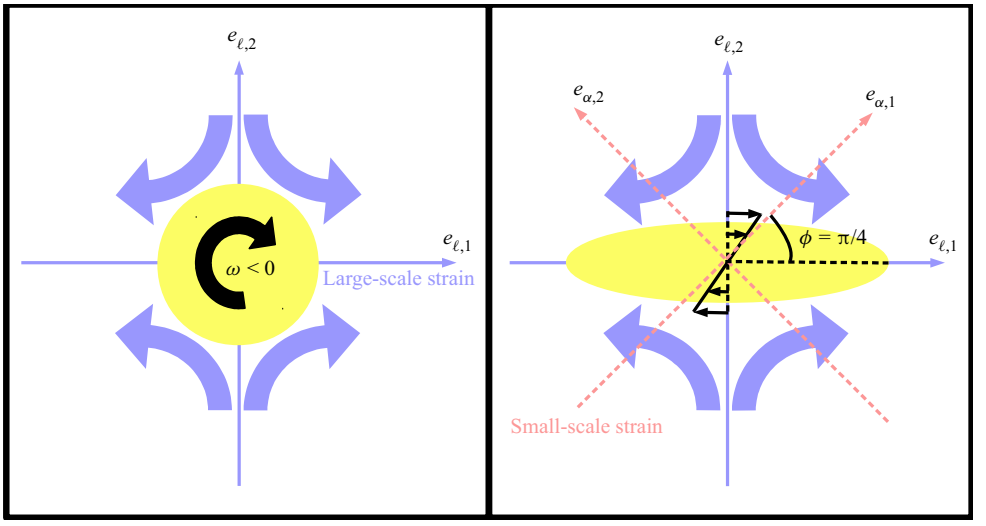

Figure 9. Simplified schematic of the vortex thinning mechanism driving an inverse energy cascade in 2-D turbulence.

self-amplification, it also demonstrates how vortex thinning could be active, even if that activity may be negligible outside a particular range of scales in practice.

In two dimensions Π_{c2} represents the inverse cascade. In the inertial range for 3-D turbulence, this vortex thinning term is evidently small compared with vorticity stretching and strain self-amplification, both of which drive a forward cascade to small scales. However, figure 8(a) also reveals that the vortex thinning term does provide a backscatter contribution for scales in between the viscous and inertial ranges, suggesting that the vortex thinning mechanism is a potential dynamical cause of the bottleneck effect.

4. Efficiency of the energy cascade

The energy cascade rate, Π^ℓ, depends on how the eigenvectors of the subfilter stress tensor align with those of the filtered strain-rate tensor (Ballouz & Ouellette 2020). This may be made explicit by writing the cascade rate in terms of eigenvalues of the filtered strain rate, λ_i, and deviatoric subfilter stress tensor, μ_j,

$$\Pi^\ell = \sum_{i=1}^{3}\sum_{j=1}^{3} \lambda_i^\ell \mu_j^\ell \cos^2(\theta_{ij}^\ell). \tag{4.1}$$

Here, θ_{ij} is the angle between the ith eigenvector of the filtered strain rate and jth eigenvector of the subfilter stress tensor. Ballouz & Ouellette (2018) defined an energy cascade efficiency as

$$\Gamma_{BO}^\ell = \frac{\Pi^\ell}{\Pi_{max,BO}^\ell}, \quad \text{where } \Pi_{max,BO}^\ell = \begin{cases} \lambda_1^\ell\mu_1^\ell + \lambda_2^\ell\mu_2^\ell + \lambda_3^\ell\mu_3^\ell & \Pi^\ell > 0 \\ -(\lambda_1^\ell\mu_3^\ell + \lambda_2^\ell\mu_2^\ell + \lambda_3^\ell\mu_1^\ell) & \Pi^\ell < 0 \end{cases} \tag{4.2}$$

is the maximum energy transfer possible for a fixed set of eigenvalues, μ_i and λ_j, for $\mathring{\boldsymbol{\tau}}^\ell$ and $\bar{\boldsymbol{S}}^\ell$, respectively. Perfect alignment between eigenvectors of the $\mathring{\boldsymbol{\tau}}^\ell$ and $\bar{\boldsymbol{S}}^\ell$ is required for an efficiency of $\Gamma^\ell = 1$. Under this definition, the average cascade efficiency is

approximately 40 % for the top-hat filter for filter widths much larger than the Kolmogorov scale (Ballouz, Johnson & Ouellette 2020).

Here, a slightly different definition of efficiency is used,

$$\Gamma^\ell = \frac{\Pi^\ell}{\Pi^\ell_{max}} = \frac{-\mathring{\boldsymbol{\tau}}^\ell : \bar{\boldsymbol{S}}^\ell}{\|\mathring{\boldsymbol{\tau}}^\ell\|\|\bar{\boldsymbol{S}}^\ell\|} = \frac{\displaystyle\sum_{i=1}^{3}\sum_{j=1}^{3}\lambda_i^\ell\mu_j^\ell\cos^2(\theta_{ij}^\ell)}{(\lambda_1^{\ell\,2}+\lambda_2^{\ell\,2}+\lambda_3^{\ell\,2})^{1/2}(\mu_1^{\ell\,2}+\mu_2^{\ell\,2}+\mu_3^{\ell\,2})^{1/2}}. \tag{4.3}$$

In addition to the re-alignment of eigenvectors, this definition of Π^ℓ_{max} in the denominator allows for the ratio of eigenvalues to be rearranged at fixed Frobenius norm to further maximize the flux. Thus, unity efficiency $\Gamma^\ell = 1$ requires not only perfect alignment of (respective) eigenvectors, $\cos^2(\theta_{ij}) = \delta_{ij}$, but also the proportionality of eigenvalues,

$$\frac{\lambda_1}{\mu_1} = \frac{\lambda_2}{\mu_2} = \frac{\lambda_3}{\mu_3}. \tag{4.4}$$

If follows that

$$\Pi^\ell_{max} \geq \Pi^\ell_{BO\,max}, \quad \text{therefore } \Gamma^\ell \leq \Gamma^\ell_{BO}. \tag{4.5}$$

It is important that $\mathring{\boldsymbol{\tau}}$ is the deviatoric part of the sub-filter stress when constructing the denominator of (4.3). This is significant because the inclusion of the isotropic part of the sub-filter stress would increase its norm without increasing the maximum potential value of its contraction with the deviatoric strain-rate tensor.

Phrasing Π^ℓ in terms of vorticity stretching and strain self-amplification, (3.7)–(3.12), allows for defining the efficiency of each dynamical mechanism in transferring energy downscale. Each component of Π^ℓ can be written as an inner product of $\bar{\boldsymbol{S}}^\ell$ with a component of the subfilter stress tensor. For example, the deviatoric part of the sub-filter stress due to single-scale strain self-amplification is

$$(\mathring{\boldsymbol{\tau}}^\ell_{s1})_{ij} = \ell^2(\bar{S}^\ell_{ik}\bar{S}^\ell_{jk} - \tfrac{1}{3}\|\bar{\boldsymbol{S}}^\ell\|^2\delta_{ij}). \tag{4.6}$$

The efficiency of the strain self-amplification, Π_{s1}, in the downscale transfer of energy is

$$\Gamma^\ell_{s1} = \frac{-\mathring{\boldsymbol{\tau}}^\ell_{s1} : \bar{\boldsymbol{S}}^\ell}{\|\mathring{\boldsymbol{\tau}}^\ell_{s1}\|\|\bar{\boldsymbol{S}}^\ell\|} = \frac{\sqrt{6}\,\Pi^\ell_{s1}}{\ell^2\|\bar{\boldsymbol{S}}^\ell\|^3} = \frac{-\sqrt{6}\,\bar{S}^\ell_{ij}\bar{S}^\ell_{jk}\bar{S}^\ell_{ki}}{\|\bar{\boldsymbol{S}}^\ell\|^3} = \frac{-3\sqrt{6}\,\lambda_1^\ell\lambda_2^\ell\lambda_3^\ell}{(\lambda_1^{\ell\,2}+\lambda_2^{\ell\,2}+\lambda_3^{\ell\,2})^{3/2}}, \tag{4.7}$$

which the reader may recognize as the s^* parameter of Lund & Rogers (1994) applied to the filtered strain-rate tensor. Thus, the strong bias of turbulence toward $\lambda_2^\ell > 0$ manifests as a bias toward positive efficiency of downscale energy flux. In fact, the PDF of s^* has been consistently shown to peak at $s^* = 1$ ($\Gamma_{s1} = 1$), i.e. $\lambda_1^\ell = \lambda_2^\ell = -\frac{1}{2}\lambda_3^\ell$. When this is true, there is one eigenvector along which the flow is strongly squeezing, with weaker stretching occurring along perpendicular directions. In the opposite case, $\Gamma^\ell_{s1} = -1$, there is strong stretching along one eigenvector and weaker squeezing along perpendicular directions, i.e. $\frac{1}{2}\lambda_1^\ell = -\lambda_2^\ell = -\lambda_3^\ell$. This situation corresponds to maximum efficiency in reverse (upscale) energy transfer and is relatively rare in turbulent flows.

Note that use of the Ballouz–Ouellette efficiency, i.e. not allowing for re-arranging of eigenvalue ratios when constructing the maximum potential flux, would result in a unity efficiency for the resolved strain self-amplification. The reason for this is that $\mathring{\boldsymbol{\tau}}^\ell_{s1}$ is, by definition, always perfectly aligned with $\bar{\boldsymbol{S}}^\ell$ so that the cascade rate by this mechanism is

only a function of the eigenvalues. This consideration was part of the reasoning motivating the definition of efficiency used here.

Another reason to use (4.3) rather than (4.2) is that the former provides a stricter test of whether the subfilter stress conforms to the eddy viscosity hypothesis, $\mathring{\tau}_{ij}^{\ell} = -2\nu_t \bar{S}_{ij}^{\ell}$. The eddy viscosity ansatz asserts that the subfilter stress not only aligns its eigenvectors with those of the filtered strain-rate tensor, but also that their eigenvalues are proportional. Thus, with the present definition of efficiency,

$$\Gamma^{\ell} = \begin{cases} 1, & \text{eddy viscosity (downscale cascade)} \\ 0, & \text{zero cascade rate} \\ -1, & \text{negative eddy viscosity (inverse cascade)} \end{cases}, \tag{4.8}$$

which can be applied individually to each term in (3.7) to test the extent to which each cascade mechanism may be accurately modelled by an eddy viscosity.

Unlike the strain self-amplification, vorticity stretching suffers from eigenvector misalignment in addition to non-optimal eigenvalue ratios. The efficiency of the energy cascade due to single-scale vorticity stretching is

$$\Gamma_{\omega 1}^{\ell} = \frac{-\mathring{\boldsymbol{\tau}}_{\omega 1}^{\ell} : \bar{\boldsymbol{S}}^{\ell}}{\|\mathring{\boldsymbol{\tau}}_{\omega 1}^{\ell}\| \|\bar{\boldsymbol{S}}^{\ell}\|} = \frac{\sqrt{6}\Pi_{\omega 1}^{\ell}}{\ell^2 \|\bar{\boldsymbol{\Omega}}^{\ell}\|^2 \|\bar{\boldsymbol{S}}^{\ell}\|} = \frac{\sqrt{6}\bar{\omega}_i^{\ell}\bar{\omega}_j^{\ell}\bar{S}_{ij}^{\ell}}{2|\bar{\boldsymbol{\omega}}^{\ell}|^2 \|\bar{\boldsymbol{S}}^{\ell}\|} = \frac{\sqrt{6}\sum_{i=1}^{3} \lambda_i^{\ell} \cos^2(\theta_{\omega,i}^{\ell})}{2(\lambda_1^{\ell 2} + \lambda_2^{\ell 2} + \lambda_3^{\ell 2})^{1/2}}, \tag{4.9}$$

where

$$(\mathring{\boldsymbol{\tau}}_{\omega 1}^{\ell})_{ij} = \ell^2(\bar{\Omega}_{ik}^{\ell}\bar{\Omega}_{jk}^{\ell} - \tfrac{1}{3}\|\bar{\boldsymbol{\Omega}}^{\ell}\|^2\delta_{ij}) = -\tfrac{1}{4}\ell^2(\bar{\omega}_i^{\ell}\bar{\omega}_j^{\ell} - \tfrac{1}{3}|\bar{\boldsymbol{\omega}}^{\ell}|^2\delta_{ij}). \tag{4.10}$$

This efficiency is maximum, $\Gamma_{\omega 1}^{\ell} = 1$, when two conditions are satisfied. First, the vorticity is perfectly aligned with the maximum eigenvalue, $\cos(\theta_{\omega,i}^{\ell}) = \delta_{i1}$. Second, the strain-rate tensor must have the configuration $\frac{1}{2}\lambda_1^{\ell} = -\lambda_2 = -\lambda_3$ so that the magnitude of the stretching is maximized. Note that the condition for maximum vorticity stretching efficiency is that of $\Gamma_{s1}^{\ell} = -1$. When $\Gamma_{s1} = 1$, the maximum efficiency of vorticity stretching is limited, $-1 \leq \Gamma_{\omega 1} \leq 0.5$. Therefore, the chaos of turbulent dynamics aside, the efficiencies of strain-rate self-amplification and vorticity stretching cannot be simultaneously maximum. In fact, the asymptotic behaviour of solutions to the restricted Euler equation as they approach the finite-time singularity is $\Gamma_{s1}^{\ell} = 1$ and $\Gamma_{\omega 1}^{\ell} = 0.5$.

The efficiencies for the multiscale terms are similarly defined and interpreted,

$$\Gamma_{s2}^{\ell} = \frac{-\mathring{\boldsymbol{\tau}}_{s2}^{\ell} : \bar{\boldsymbol{S}}^{\ell}}{\|\mathring{\boldsymbol{\tau}}_{s2}^{\ell}\| \|\bar{\boldsymbol{S}}^{\ell}\|}, \quad \Gamma_{\omega 2} = \frac{-\mathring{\boldsymbol{\tau}}_{\omega 2}^{\ell} : \bar{\boldsymbol{S}}^{\ell}}{\|\mathring{\boldsymbol{\tau}}_{\omega 2}^{\ell}\| \|\bar{\boldsymbol{S}}^{\ell}\|}, \quad \Gamma_{c}^{\ell} = \frac{-\mathring{\boldsymbol{\tau}}_{c}^{\ell} : \bar{\boldsymbol{S}}^{\ell}}{\|\mathring{\boldsymbol{\tau}}_{c}^{\ell}\| \|\bar{\boldsymbol{S}}^{\ell}\|}. \tag{4.11a–c}$$

In terms of filtered strain-rate eigenvalues, λ_i^{ℓ}, subfilter stress eigenvalues, $\mu_{x,j}$, and eigenvector alignment angles, $\theta_{x,ij}$, the efficiencies of the multiscale cascade rates are

$$\Gamma_{x}^{\ell} = \frac{\sum_{i=1}^{3}\sum_{j=1}^{3} \lambda_i^{\ell}\mu_{x,j}^{\ell} \cos^2(\theta_{x,ij}^{\ell})}{(\lambda_1^{\ell 2} + \lambda_2^{\ell 2} + \lambda_3^{\ell 2})^{1/2}(\mu_{x,1}^{\ell\ 2} + \mu_{x,2}^{\ell\ 2} + \mu_{x,3}^{\ell\ 2})^{1/2}}, \quad \text{where } x = s2, \omega 2, c. \tag{4.12}$$

The average cascade efficiencies from DNS of HIT are shown in figure 10(*a*) as a function of filter width. At a filter width chosen in the middle of the inertial range, $\ell = 46\eta$,

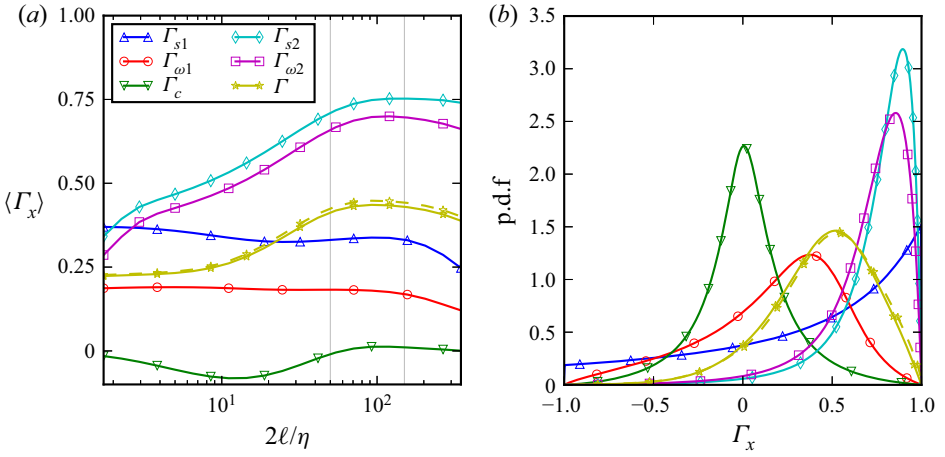

Figure 10. Cascade efficiencies for each term in (3.7): (*a*) average efficiency as a function of filter width and (*b*) PDF of efficiency at $\ell = 46\eta$. The dashed line shows the Ballouz–Ouellette efficiency.

the PDF of each term is also shown in figure 10(*b*). The overall cascade efficiency is less than 25 % in the viscous range and grows above 40 % in the inertial range. The overall efficiency based the Ballouz–Ouellette definition is only slightly larger than the present one. The PDF of the total cascade rate peaks near 50 %, and negative efficiencies below −50 % extremely rare. Indeed, the eddy viscosity approximation for subfilter stresses lacks a high degree physical fidelity in general.

The single-scale terms, Π_{s1} and $\Pi_{\omega 1}$, are less efficient than the total subfilter activity in supporting a downscale cascade in the inertial range. In fact, their efficiency is relatively constant as a function of scale from the viscous range through the inertial range. The strain self-amplification efficiency PDF peaks at $\Gamma_{s1}^{\ell} = 1$, but also allows for substantial negative efficiencies. Meanwhile, the most commonly observed efficiency for single-scale vorticity stretching is slightly less than 50 %, but negative efficiencies for this mechanism are also not particularly rare. Thus, the signature of restricted Euler dynamics is observed in the location of the efficiency PDF peaks, namely, at $\Gamma_{s1}^{\ell} = 1$ and $\Gamma_{\omega 1}^{\ell} = 0.5$. Nevertheless, the mean efficiency is quite low due to the fluctuations.

In contrast, the three multiscale processes have more sharply peaked efficiency PDFs. Multiscale vorticity stretching and strain self-amplification show a strong tendency toward eddy viscosity-like behaviours, with mean efficiencies near 70 % and 75 %, respectively, in the inertial range. Indeed these terms rarely generate backscatter, and when they do, it is inefficient in alignment. While the restricted Euler dynamics may be invoked for the single-scale terms, the smaller-scale strain rates and vorticities comprising $\mathring{\boldsymbol{\tau}}_{s2}^{\ell}$ and $\mathring{\boldsymbol{\tau}}_{\omega 2}^{\ell}$ evolve on faster time scales compared with $\bar{\boldsymbol{S}}^{\ell}$, coming closer to satisfying conditions of scale separation that leads to eddy viscosity physics. It is known, for example, that finer-scale vorticity aligns more readily with the strongest extensional direction of a larger-scale strain rate (Leung *et al.* 2012; Fiscaletti *et al.* 2016), which is physically related to the time lag in alignment elucidated by Xu, Pumir & Bodenschatz (2011). The Lagrangian behaviour of these terms deserves further consideration in future work.

The PDF of the strain–vorticity covariance term, Π_c, is also strongly peaked. Unlike the vorticity stretching and strain self-amplification terms, the most common value of Π_c is zero. The PDF is symmetric and the mean value is very small throughout the inertial range. While it is does not appear correlated with $\bar{\boldsymbol{S}}^{\ell}$, it is not known whether $\mathring{\boldsymbol{\tau}}_{c2}$ is

strongly correlated with other quantities filtered at scale ℓ to facilitate LES modelling of this term.

5. Scale locality of the energy cascade

It has been presumed in the discussion so far that the interscale energy transfer in turbulence may be faithfully characterized as a cascade. However, it is useful to leverage the present developments to examine the scale locality of energy transfer. A distinct advantage of (3.7) is that its formulation allows this question to be addressed in the context of vorticity stretching and strain self-amplification mechanisms.

Scale locality of the cascade can be quantified by computing the energy transfer across scale ℓ that remains resolved when the velocity field is filtered at scale $0 \leq \ell' \leq \ell$, here denoted $\Pi^{\ell,\ell'}$. That is, the energy cascade rate at ℓ is computed in the artificial absence of any motions smaller than scale ℓ'. When $\ell' = 0$, it is trivial that 100 % of the interscale energy transfer will be resolved, $\Pi^{\ell,0} = \Pi^{\ell}$. On the other hand, if $\ell' = \ell$, then the resolved energy transfer is $\Pi^{\ell,\ell'} = \Pi^{\ell}_{s1} + \Pi^{\ell}_{\omega 1}$. It is evident from figure 8(*a*) that this accounts for roughly 50 % of the total $\langle \Pi^{\ell} \rangle$. The question of scale locality, then, is how quickly $\Pi^{\ell,\ell'}$ approaches Π^{ℓ} when ℓ' is decreased below ℓ.

First, a brief mathematical development is presented to generate the expressions needed to quantitatively evaluate the question of scale locality outlined in words in the previous paragraph. Given (3.4), the sub-filter stress tensor may be written as

$$\tau_{\ell}(u_i, u_j) = \int_0^{\ell^2} \mathrm{d}\alpha \overline{\bar{A}_{ik}^{\sqrt{\alpha}} \bar{A}_{jk}^{\sqrt{\alpha}}}^{\beta}, \tag{5.1}$$

where $\beta = \sqrt{\ell^2 - \alpha}$. Supposing the velocity field was known only to resolution $0 \leq \ell' \leq \ell$, then the resolved amount of sub-filter stress would be

$$\tau_{\ell,\ell'}(u_i, u_j) = \int_{\ell'^2}^{\ell^2} \mathrm{d}\alpha \overline{\bar{A}_{ik}^{\sqrt{\alpha}} \bar{A}_{jk}^{\sqrt{\alpha}}}^{\beta} + \int_0^{\ell'^2} \mathrm{d}\alpha \overline{\bar{A}_{ik}^{\ell'} \bar{A}_{jk}^{\ell'}}^{\sqrt{\ell^2 - \ell'^2}}, \tag{5.2}$$

because, for $\alpha < \ell'^2$, the integrand is not fully known and the velocity gradients filtered at scale $\sqrt{\alpha}$ can at best be approximated by the velocity gradients filtered at scale ℓ'. Subtracting (5.2) from (5.1) results in an equation for the unresolved sub-filter stress,

$$\tau_{\ell}(u_i, u_j) - \tau_{\ell,\ell'}(u_i, u_j) = \int_0^{\ell'^2} \mathrm{d}\alpha \overline{\tau_{\beta'}(\bar{A}_{ik}^{\sqrt{\alpha}}, \bar{A}_{jk}^{\sqrt{\alpha}})}^{\sqrt{\ell^2 - \ell'^2}}, \tag{5.3}$$

where $\beta' = \sqrt{\ell'^2 - \alpha}$. Contracting (5.3) with the filtered strain-rate tensor, $\bar{\boldsymbol{S}}^{\ell}$, defines the unresolved portion of Π^{ℓ} for a velocity field filtered at scale ℓ'. Figure 11(*a*) shows this quantity computed from DNS results. The top curve shows the result for $\ell' = \ell$. It is evident that the interscale transfer has at least some degree of locality, because these curves drop steeply from their originating points on the black $\ell' = \ell$ curve.

Following Eyink (2005), a power-law relation may be expected,

$$\chi^{\ell,\ell'} = \frac{\langle \Pi^{\ell} - \Pi^{\ell,\ell'} \rangle}{\langle \Pi^{\ell} \rangle} \sim \left(\frac{\ell'}{\ell} \right)^{p}. \tag{5.4}$$

The exponent p quantifies the extent of scale locality. A steeper power law means a higher degree of scale-local dominance and more adherence to cascade-like behaviour. A log–log

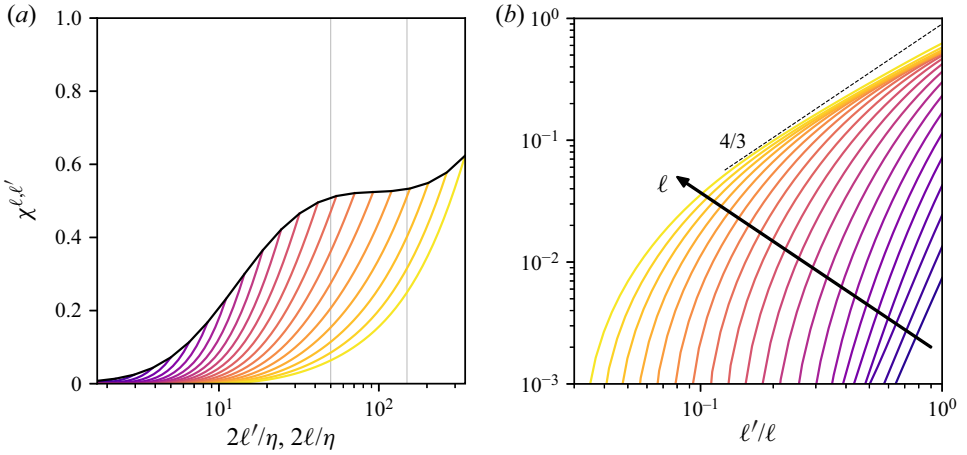

Figure 11. (*a*) Per cent of unresolved cascade rate when the velocity field is filtered at scale $\ell' \leq \ell$, for various ℓ. Top (black) curve indicates results for $\ell' = \ell$. The (coloured) curves emanating downward from the top curve show results for $\ell' < \ell$, each curve representing a different fixed value of ℓ (the value at which it intersects the black curve). (*b*) The same results (with same corresponding colours) plotted log–log as a function of ℓ'/ℓ, each curve again representing a different fixed value of ℓ. The dashed line indicates the theoretical power-law exponent of 4/3.

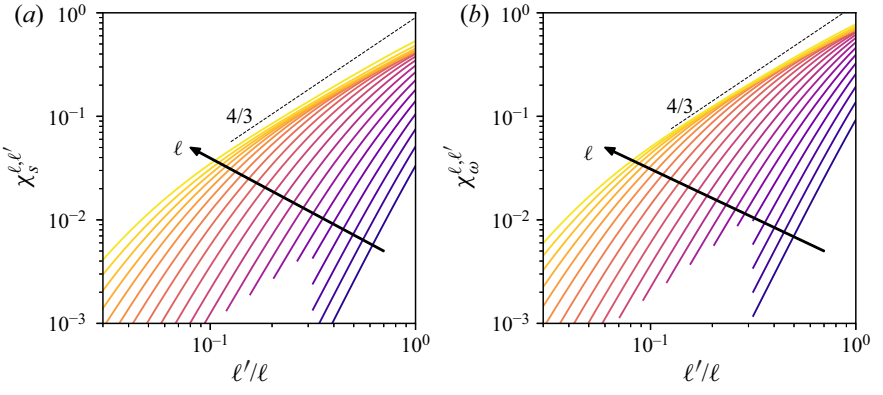

Figure 12. Per cent of (*a*) $\langle \Pi_s^\ell \rangle = \langle \Pi_{s1}^\ell + \Pi_{s2}^\ell \rangle$ and (*b*) $\langle \Pi_\omega^\ell \rangle = \langle \Pi_{\omega 1}^\ell + \Pi_{\omega 2}^\ell \rangle$ unresolved by velocity field filtered at scale $\ell' \leq \ell$ plotted log–log against ℓ'/ℓ, as in figure 11(*b*). The dashed lines indicates a power-law exponent of 4/3. The value of ℓ corresponding to each colour is the same as in figure 11.

plot of the unresolved component of interscale energy transfer is shown in figure 11(*b*). For large enough ℓ and ℓ', the curves appear to collapse as would be a good indicator of scale-invariant behaviour. Furthermore, the power-law curve fit produces an exponent near 1.1 for the overlapping region of the orange-ish curves. This deviates some from the theoretical prediction of 4/3, though it is certainly steeper than a 2/3 power law which would result from perfect correlation across scales (Eyink 2005; Eyink & Aluie 2009). This result suggests that current theories may over-estimate the de-correlation effect. A more precise estimate of this power law requires higher resolution DNS.

The current formulation allows us to follow this line of investigation further. Specifically, the above decomposition into resolved and unresolved components of the

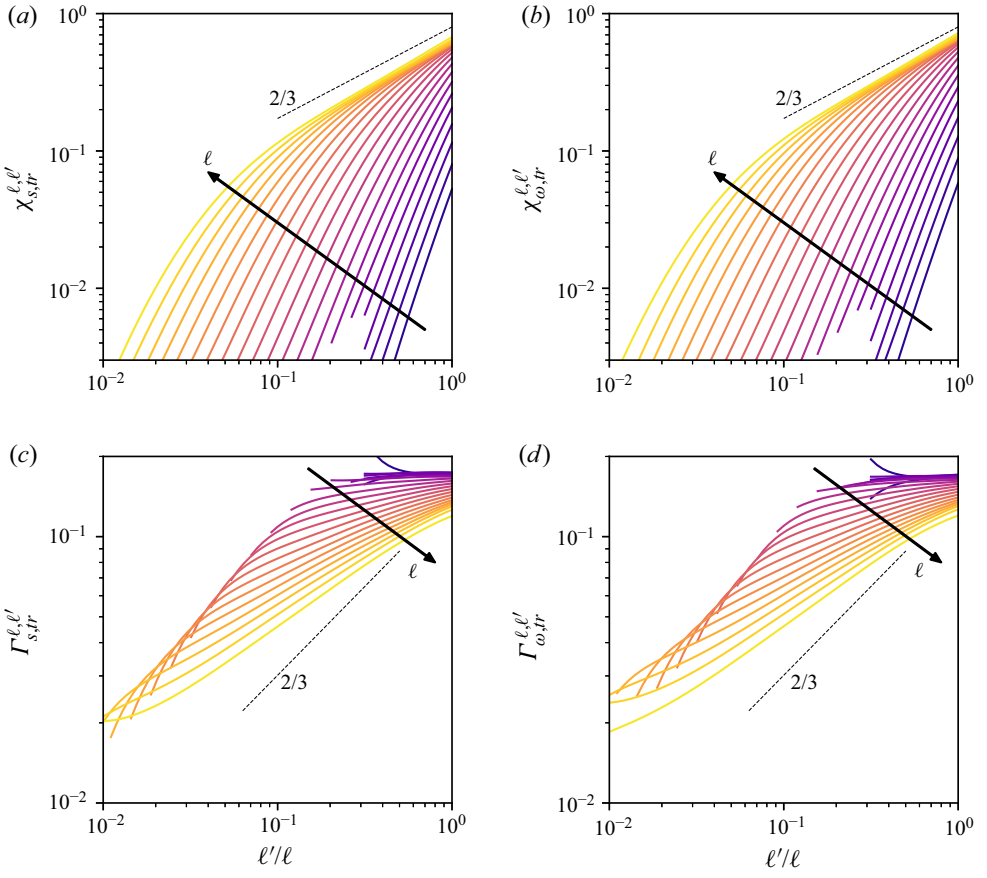

Figure 13. Trace of the subfilter stress tensor at scale ℓ remaining unresolved at scale ℓ', as a function of ℓ'/ℓ for various values of $0.9\eta \leq \ell \leq 170\eta$: (*a*) unresolved strain-rate component, (*b*) unresolved vorticity component. Also, trace-based cascade efficiency of the unresolved subfilter stress: (*c*) unresolved strain-rate component, (*d*) unresolved vorticity component. The value of ℓ corresponding to each colour is the same as in figure 11.

interscale energy transfer may be performed separately for strain self-amplification and vorticity stretching. Mathematically, this is done by replacing the full velocity gradient tensor in (5.1)–(5.3) with either its symmetric or anti-symmetric part,

$$\chi_s^{\ell,\ell'} = \frac{\langle \Pi_s^{\ell} - \Pi_s^{\ell,\ell'} \rangle}{\langle \Pi_s^{\ell} \rangle}, \quad \chi_\omega^{\ell,\ell'} = \frac{\langle \Pi_\omega^{\ell} - \Pi_\omega^{\ell,\ell'} \rangle}{\langle \Pi_\omega^{\ell} \rangle}. \tag{5.5a,b}$$

The results for strain self-amplification and vorticity stretching are qualitatively similar to figure 11(*a*). In figure 12, each of these two are shown on a log–log plot vs ℓ'/ℓ. Similar collapse into power-law behaviour is seen. This indicates that strain self-amplification and vorticity stretching have very similar scale-locality properties when it comes to their contributions to the energy cascade, each one very similar to the $p \approx 1.1$ behaviour of the total cascade rate.

To further explore the observed discrepancy with theoretical predictions, the efficiency of the unresolved subfilter stress is computed as a function of ℓ' for each filter width ℓ. This decomposes the decay of the unresolved portion of Π to be split into decreasing magnitude

and de-correlation with $\bar{\boldsymbol{S}}^{\ell}$. The theory predicts a power-law decay of $2/3$ for each. To fully accomplish this, a slightly altered definition of efficiency is needed. In particular, to measure the de-correlation effect, the denominator of efficiency should use the trace of the unresolved subfilter stress tensor rather than the norm of its deviatoric part,

$$\Gamma^{\ell,\ell'}_{s,tr} = \frac{-(\boldsymbol{\tau}^{\ell}_{s} - \boldsymbol{\tau}^{\ell,\ell'}_{s}) : \bar{\boldsymbol{S}}^{\ell}}{\mathrm{tr}(\boldsymbol{\tau}^{\ell}_{s} - \boldsymbol{\tau}^{\ell,\ell'}_{s})\|\bar{\boldsymbol{S}}^{\ell}\|}, \quad \Gamma^{\ell,\ell'}_{\omega,tr} = \frac{-(\boldsymbol{\tau}^{\ell}_{\omega} - \boldsymbol{\tau}^{\ell,\ell'}_{\omega}) : \bar{\boldsymbol{S}}^{\ell}}{\mathrm{tr}(\boldsymbol{\tau}^{\ell}_{\omega} - \boldsymbol{\tau}^{\ell,\ell'}_{\omega})\|\bar{\boldsymbol{S}}^{\ell}\|}. \tag{5.6a,b}$$

Indeed, a perfectly decorrelated stress tensor in the physical sense could be an isotropic tensor. In other words, it is not desired to measure the extent to which the deviations from an isotropic tensor align with the filtered strain rate, but rather, how much energy transfer is occurring for a given level of subfilter activity.

The results are shown in figure 13. Panels (*a,b*) show the decay of the unresolved trace for strain-rate amplification and vorticity stretching,

$$\chi^{\ell,\ell'}_{s,tr} = \frac{\mathrm{tr}(\boldsymbol{\tau}^{\ell}_{s} - \boldsymbol{\tau}^{\ell,\ell'}_{s})}{\mathrm{tr}(\boldsymbol{\tau}^{\ell}_{s})}, \quad \chi^{\ell,\ell'}_{\omega,tr} = \frac{\mathrm{tr}(\boldsymbol{\tau}^{\ell}_{\omega} - \boldsymbol{\tau}^{\ell,\ell'}_{\omega})}{\mathrm{tr}(\boldsymbol{\tau}^{\ell}_{\omega})}. \tag{5.7a,b}$$

Below these, the respective decay of efficiency is shown, (5.6*a,b*). Panels (*c,d*) show the same results for vorticity stretching. For both mechanisms, the $2/3$ power law is observed for the trace but the efficiency decays more slowly than predicted by theory. However, the results suggest that the decorrelation (efficiency decay) becomes steeper as ℓ increases. It is plausible, then, that a simulation with a significantly higher Reynolds number may produce results in better agreement with theory at sufficiently large ℓ/η. At the very least, the present results do no rule out that possibility. It is worth noting that Domaradzki *et al.* (2009) observed results consistent with $p = 4/3$ using a Fourier decomposition, but also had technical difficulties due to finite Reynolds number DNS.

6. Conclusion

In this paper, the exact relationship introduced by Johnson (2020*a*) is exploited to discern the role of strain-rate amplification and vorticity stretching in transferring kinetic energy from large to small scales in turbulent flows. About half of the net energy cascade rate is proportional to velocity gradient production rates. These rates, which can be described as vorticity stretching and strain self-amplification of the filtered field, have important statistical biases which contain the signature of the restricted Euler dynamics. For instance, the tendency toward a strain-rate eigenvalue state or $\lambda_1 = \lambda_2 = -\frac{1}{2}\lambda_3$ makes strain self-amplification more efficient at driving the cascade while limiting the efficiency of vorticity stretching. Indeed, the efficiency PDFs indicate a tendency of turbulent dynamics to favour restricted Euler-like alignments. However, the pressure is also evidently important in determining average cascade rates. The pressure imposes the divergence-free condition, $\boldsymbol{\nabla} \cdot \boldsymbol{u}$, one consequence of which is the three-to-one ratio between average strain self-amplification and vorticity stretching rates. Thus, both the autonomous dynamics of the velocity gradient and the non-local action of the pressure favour energy cascade via strain self-amplification over vortex stretching, in terms of efficiency and average rate, respectively. This work joins Carbone & Bragg (2020) and Vela-Martín & Jiménez (2021) in highlighting the crucial role of strain-rate self-amplification in the energy cascade, calling into question the classical emphasis on vorticity stretching (Taylor 1938; Onsager 1949).

Note that this conclusion about the relative contributions is for the average cascade rate and does not contradict the observation by others that vorticity stretching is more influential in generating extreme events in turbulent flows (Buaria *et al.* 2019; Carbone & Bragg 2020). Another point of nuance not yet pursued is a possible subtle difference between vortex stretching and vorticity stretching. Indeed, regions of strong vorticity are often positioned close to regions of strong strain (Vlaykov & Wilczek 2019), so that the stretching of a vortex, if more broadly conceived of as the evolution of a flow structure that also includes regions of higher strain rate, may include the strain self-amplification as defined mathematically in this paper. In general, further investigation of the Johnson (2020*a*) formulation in terms of spatially coherent structures would be insightful (Dong *et al.* 2020).

A significant advantage of the formulation from Johnson (2020*a*) is the ability to write the remainder of the energy cascade rate in terms of multiscale vorticity stretching and strain-rate amplification mechanisms. It is shown in this paper that the stretching of smaller-scale vorticity and the amplification of smaller-scale strain rate by larger-scale strain rate is responsible for the other half of the energy cascade rate. These subfilter stress components are more efficiently aligned with the filtered strain-rate tensor, proving to be better approximated using an eddy viscosity. The net contribution of multiscale interactions decreases with scale separation as a power law, in close agreement to theoretical $4/3$ power-law predictions for the scale locality of interscale energy transfer. This is true for both strain self-amplification and vorticity stretching mechanisms. Note that this is still not a particularly strong degree of locality, especially when compared with, e.g. the bubble breakup cascade in two-phase turbulent flows, where a much steeper power law is predicted and observed (Chan, Johnson & Moin 2020*a*; Chan *et al.* 2020*b*).

Finally, a third cascade mechanism is explored, namely, the distortion of small-scale strain–vorticity covariance by the larger-scale strain rate. While the net contribution of this term is negligible in the inertial range of 3-D turbulence, it has noticeable effects elsewhere. In two dimensions, it is the only possible mechanism, because both strain-rate amplification and vorticity stretching vanish exactly. This mechanism is responsible for the inverse cascade in two dimensions. It is argued, following Chen *et al.* (2006) and Xiao *et al.* (2009), that this term may be interpreted as a vortex thinning mechanism (Kraichnan 1976). Furthermore, in three dimensions, the strain–vorticity correlation drives net backscatter opposing strain self-amplification and vorticity stretching for a range of filter width between viscous and inertial scales. This is the range of scales where the so-called spectral bump occurs, advancing vortex thinning as a candidate mechanism for what causes the bottleneck effect in three dimensions.

Velocity increments and structure functions have featured heavily in turbulence theory. No doubt, the ease of measurement using hot-wire anemometry (provided one may assume Taylor's hypothesis) has fuelled the use of such two-point statistics. Filtered velocity gradients naturally encompass the information contained in velocity increments and similarly enable a scale-by-scale investigation of turbulent flows. The advantage of filtered velocity gradients is the ability to distinguish solid-body rotation from fluid deformation organized at scales much larger than η. Writing interscale energy transfer in terms of filtered velocity gradients not only connects with (and expands upon) classical cascade descriptions in terms of vorticity stretching, but also leverages the insights of the restricted Euler equation. A natural connection emerges between turbulence theory and modelling for LES, a tool of increasing practical importance in the age of supercomputing.

Acknowledgements. A. Elnahhas is acknowledged for providing helpful feedback on an initial draft of this manuscript. The author benefited from discussions on this topic with a number of colleagues, in alphabetical

order by last name: J. Ballouz, A. Bragg, J. Cardesa, G. Eyink, S. Lele, A. Lozano-Duran, P. Moin, N. Ouellette and I. Paul.

Funding. This work was supported in part by the Advanced Simulation and Computing program of the U.S. Department of Energy's National Nuclear Security Administration via the PSAAP-II Grant no. DE-NA0002373.

Declaration of interests. The author reports no conflict of interest.

Author ORCIDs.
Perry L. Johnson https://orcid.org/0000-0002-7929-9396.

Appendix A. Relative importance of the small-scale strain–vorticity covariance

In (3.7), the first two terms, $\mathring{\boldsymbol{\tau}}_{s1}$ and $\mathring{\boldsymbol{\tau}}_{\omega 1}$, are resolved at scale ℓ. Therefore, in theory, these two need no approximate modelling for LES. The third and fourth terms, $\mathring{\boldsymbol{\tau}}_{s2}$ and $\mathring{\boldsymbol{\tau}}_{\omega 2}$, have been shown to be better approximated by an eddy viscosity, figure 10. The fifth term, which may be thought of as a vortex thinning term, $\mathring{\boldsymbol{\tau}}_{c2}$, is not so easily modelled. The simplest model would be to ignore its contribution, which is close to zero in the mean within the inertial range of scales.

A preliminary *a priori* study of the effects of neglecting some of the terms in (3.7) is shown in figure 14. As previously shown by Borue & Orszag (1998), the correlation coefficient of the tensor diffusivity model, $\Pi \approx \Pi_{s1} + \Pi_{\omega 1}$, is quite good, near 0.9 in the inertial range. The normalized mean square error, R^2, is around 0.75. When the multiscale vorticity stretching and strain self-amplification terms are added as well, $\Pi \approx \Pi_{s1} + \Pi_{\omega 1} + \Pi_{s2} + \Pi_{\omega 2}$, the correlation coefficient exceeds 0.95 and the R^2 value also significantly improves. This observation provides evidence that (3.7) is a meaningful decomposition of the energy cascade rate, because the accuracy of the sum improves as more terms are included. The correlation coefficients and R^2 values are perfect, 1.0, when all five terms are included in the sum, reflecting the exact nature of (3.7) on a point-wise basis. This point-wise verification was also performed for the full tensor, (3.4), with relative errors comparable to machine precision. There is also some error associated with the trapezoidal rule integration, though this component of the error is made small through refinement of $\Delta\alpha$.

Appendix B. Cascade rate and efficiency PDFs as a function of scale

The mean cascade rate, Π^ℓ, and cascade efficiency, Γ^ℓ, were shown as a function of ℓ/η in figures 8(*a*) and 10(*a*), respectively. In the inertial range, $50 \lessapprox 2\ell/\eta \lessapprox 150$, these mean quantities were relatively flat indicating some degree of scale similarity. Alongside these mean values, figures 8(*b*) and 10(*b*) show the PDFs for cascade rate and efficiency at a single filter width in the middle of the inertial range, $2\ell/\eta \approx 92$. In this Appendix, more plots are included to explore the dependence of the PDFs on the filter width.

Figure 15(*a*) shows the PDFs for the total cascade efficiency for six different filter widths. The remaining five panels, figure 15(*b–f*), show the cascade efficiency PDFs for each of the five terms on the right side of (3.7). The largest three filter widths shown are in the approximate inertial range and their PDFs are remarkably similar. Some minor deviation is observed for $2\ell/\eta = 54$ at the lower end of the inertial range. This observation further supports the identification of inertial range scales in the simulation.

Further, the efficiency PDFs of the two single-scale cascade mechanisms, Γ_{s1} and $\Gamma_{\omega 1}$, show little variation between inertial and viscous range filter widths. The reason for this is the similarity in velocity gradient tensor tendencies regardless of filter scale. The second

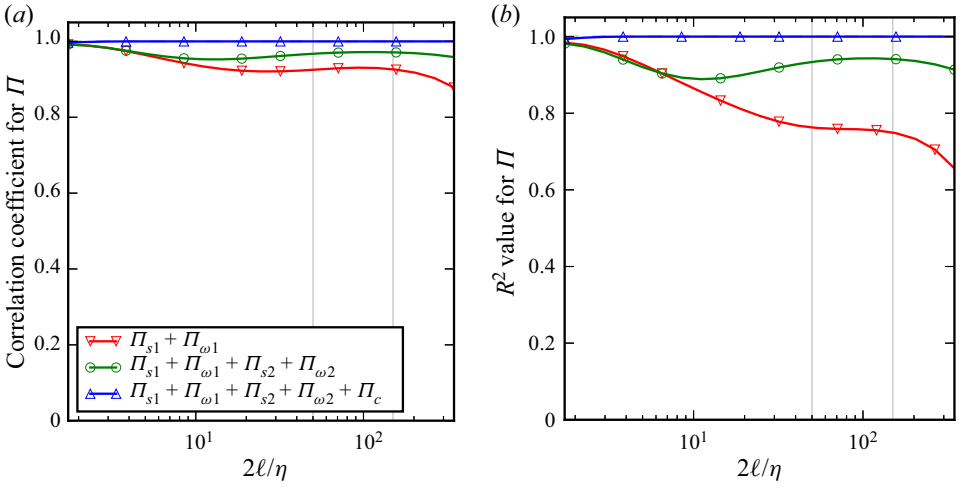

Figure 14. Correlation coefficient (*a*) and mean square error (*b*) for complete and incomplete sums of the cascade mechanisms.

derivative of the subfilter stress tensor, being the dynamical difference between velocity gradients filtered at different scales, evidently does not play a major role in altering these efficiencies. In contrast, the three multiscale contributions to the cascade have significantly different PDFs in the viscous range than observed at larger filter widths.

While similarity is clearly observed in the inertial range for the efficiency PDFs, the same cannot be said of the cascade rates themselves, figure 16. As the energy cascade progresses to smaller scales, the phenomenon of intermittency manifests in increasingly heavy-tailed distributions of the cascade rate. This is true for the total cascade rate as well as each of the five different contributions on the right side of (3.7). Within the viscous range, the PDFs do start to collapse to some extent, but less so for the multiscale rates. However, the decrease in available active subfilter scales easily explains this fact.

Appendix C. Detailed derivation of energy cascade rate for Gaussian filters

For any field variable, $a(\boldsymbol{x})$, with Fourier transform, $\mathcal{F}\{a\}(\boldsymbol{k})$, the Gaussian filtered field is

$$\mathcal{F}\{\bar{a}^\ell\}(\boldsymbol{k}) = \exp(-\tfrac{1}{2}k^2\ell^2)\mathcal{F}\{a\}(\boldsymbol{k}), \tag{C1}$$

which by substitution is seen to satisfy

$$\frac{\partial \mathcal{F}\{\bar{a}^\ell\}}{\partial(\ell^2)} = -\frac{1}{2}k^2\mathcal{F}\{\bar{a}^\ell\}. \tag{C2}$$

This equation is the Fourier transform of

$$\frac{\partial \bar{a}^\ell}{\partial(\ell^2)} = \frac{1}{2}\nabla^2\bar{a}^\ell \tag{C3}$$

and the initial condition, $\bar{a}^{\ell=0}(\boldsymbol{x}) = a(\boldsymbol{x})$, is satisfied.

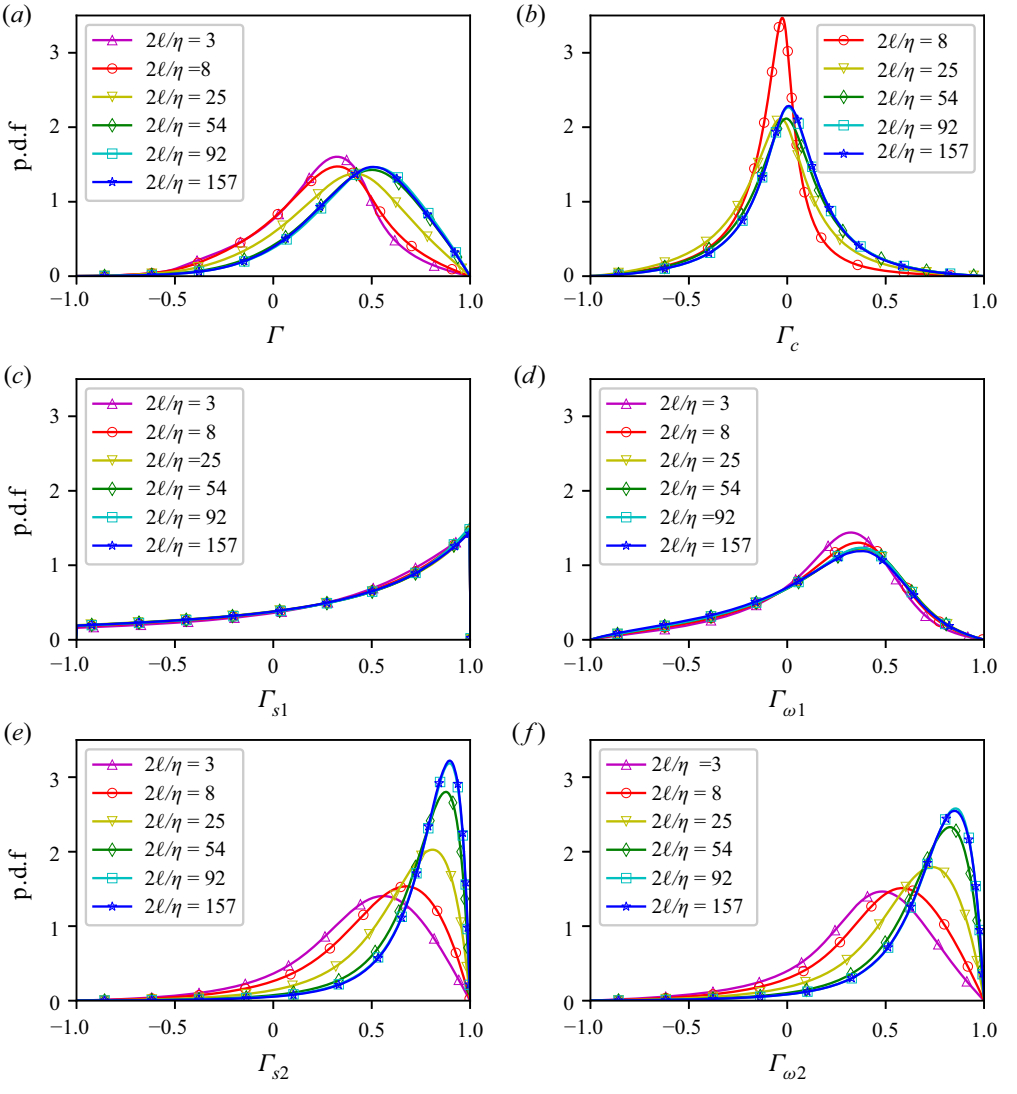

Figure 15. PDFs for the cascade efficiencies at various filter widths: (*a*) total cascade efficiency, (*b*) strain–vorticity covariance amplification, (*c*) single-scale strain-rate self-amplification, (*d*) single-scale vorticity stretching, (*e*) multiscale strain-rate amplification and (*f*) multiscale vorticity stretching.

Now the generalized second moment of two fields, $a(\boldsymbol{x})$ and $b(\boldsymbol{x})$ may be written as

$$\tau_\ell(a,b) = \overline{ab}^\ell - \bar{a}^\ell \bar{b}^\ell \tag{C4}$$

and its derivative with ℓ^2 is

$$\frac{\partial \tau_\ell(a,b)}{\partial(\ell^2)} = \frac{\partial \overline{ab}^\ell}{\partial(\ell^2)} - \left(\bar{a}^\ell \frac{\partial \bar{b}^\ell}{\partial(\ell^2)} + \bar{b}^\ell \frac{\partial \bar{a}^\ell}{\partial(\ell^2)}\right). \tag{C5}$$

Now substituting (C3) for all three derivatives in ℓ^2 on the right side,

$$\frac{\partial \tau_\ell(a,b)}{\partial(\ell^2)} = \frac{1}{2}\nabla^2 \overline{ab}^\ell - \frac{1}{2}(\bar{a}^\ell \nabla^2 \bar{b}^\ell + \bar{b}^\ell \nabla^2 \bar{a}^\ell) \tag{C6}$$

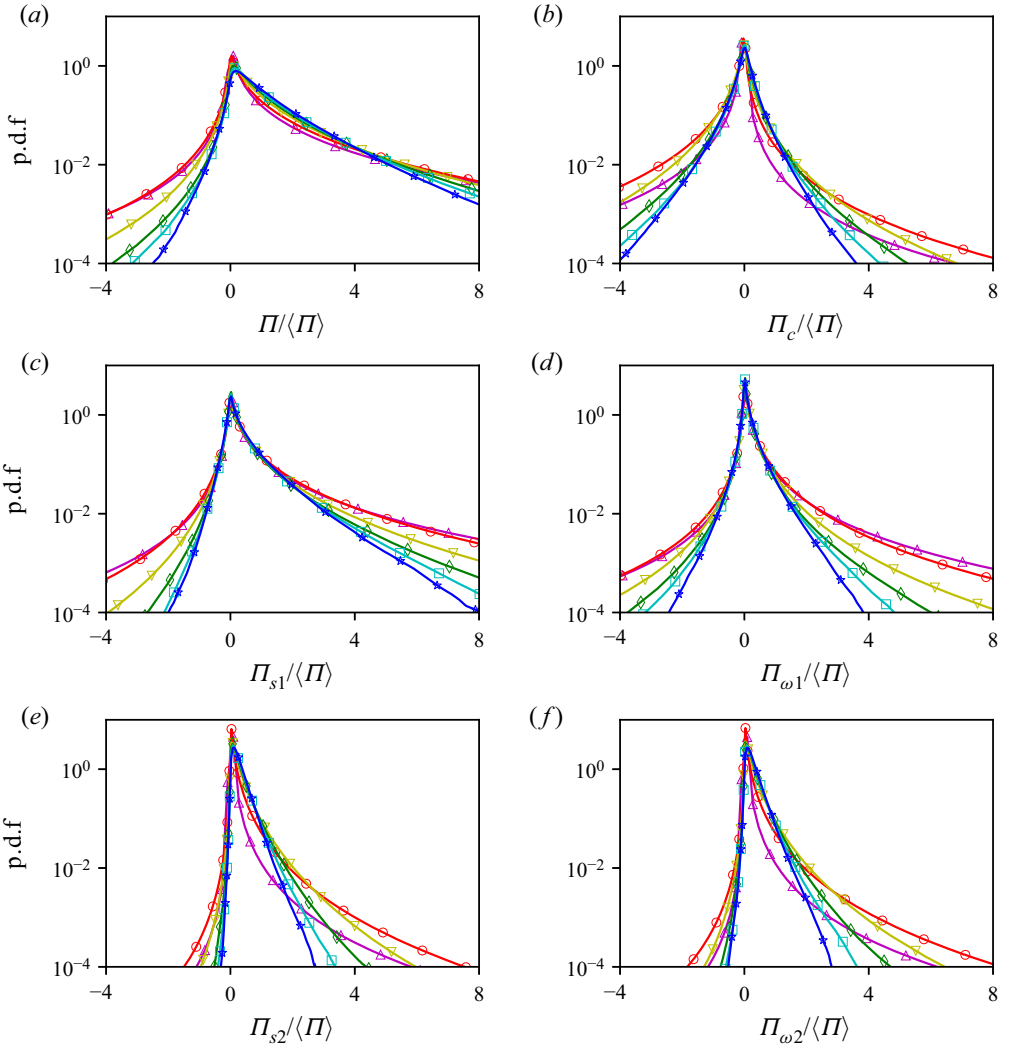

Figure 16. PDFs for the cascades rates at various filter widths: (*a*) total cascade efficiency, (*b*) strain–vorticity covariance amplification, (*c*) single-scale strain-rate self-amplification, (*d*) single-scale vorticity stretching, (*e*) multiscale strain-rate amplification and (*f*) multiscale vorticity stretching. The legend from figure 15 also applies here.

and using the product rule, the following relationship may be established

$$\nabla^2(\bar{a}^\ell \bar{b}^\ell) = \bar{a}^\ell \nabla^2 \bar{b}^\ell + \bar{b}^\ell \nabla^2 \bar{a}^\ell + 2\frac{\partial \bar{a}^\ell}{\partial x_j}\frac{\partial \bar{b}^\ell}{\partial x_j}, \tag{C7}$$

which upon substitution yields,

$$\frac{\partial \tau_\ell(a,b)}{\partial(\ell^2)} = \frac{1}{2}\nabla^2(\overline{ab}^\ell - \bar{a}^\ell \bar{b}^\ell) + \frac{\partial \bar{a}^\ell}{\partial x_j}\frac{\partial \bar{b}^\ell}{\partial x_j}, \tag{C8}$$

hence

$$\frac{\partial \tau_\ell(a,b)}{\partial(\ell^2)} = \frac{1}{2}\nabla^2 \tau_\ell(a,b) + \frac{\partial \bar{a}^\ell}{\partial x_j}\frac{\partial \bar{b}^\ell}{\partial x_j}. \tag{C9}$$

Note that, by definition, $\tau_{\ell=0}(a,b)=0$. The Fourier transform of this equation is

$$\frac{\partial \mathcal{F}\{\tau_\ell(a,b)\}}{\partial(\ell^2)} = -\frac{1}{2}k^2\mathcal{F}\{\tau_\ell(a,b)\} + \mathcal{F}\left\{\frac{\partial \bar{a}^\ell}{\partial x_j}\frac{\partial \bar{b}^\ell}{\partial x_j}\right\}. \tag{C10}$$

Multiplying by $\exp(\frac{1}{2}k^2\ell^2)$,

$$\frac{\partial}{\partial(\ell^2)}\left[\exp\left(\frac{1}{2}k^2\ell^2\right)\mathcal{F}\{\tau_\ell(a,b)\}\right] = \exp\left(\frac{1}{2}k^2\ell^2\right)\mathcal{F}\left\{\frac{\partial \bar{a}^\ell}{\partial x_j}\frac{\partial \bar{b}^\ell}{\partial x_j}\right\} \tag{C11}$$

and integrating with dummy variable α from 0 to ℓ^2,

$$\exp\left(\frac{1}{2}k^2\ell^2\right)\mathcal{F}\{\tau_\ell(a,b)\} = \int_0^{\ell^2}\exp\left(\frac{1}{2}k^2\alpha\right)\mathcal{F}\left\{\overline{\frac{\partial a}{\partial x_j}}^{\sqrt{\alpha}}\overline{\frac{\partial b}{\partial x_j}}^{\sqrt{\alpha}}\right\}\mathrm{d}\alpha, \tag{C12}$$

where $\tau_{\ell=0}(a,b)=0$ has been used on the left side of the equation. Then dividing by $\exp(\frac{1}{2}k^2\ell^2)$ solving for the generalized second moment,

$$\mathcal{F}\{\tau_\ell(a,b)\} = \int_0^{\ell^2}\exp\left[-\frac{1}{2}k^2(\ell^2-\alpha)\right]\mathcal{F}\left\{\overline{\frac{\partial a}{\partial x_j}}^{\sqrt{\alpha}}\overline{\frac{\partial b}{\partial x_j}}^{\sqrt{\alpha}}\right\}\mathrm{d}\alpha, \tag{C13}$$

which can be written as a Gaussian filter with width $\sqrt{\ell^2-\alpha}$,

$$\mathcal{F}\{\tau_\ell(a,b)\} = \int_0^{\ell^2}\mathcal{F}\left\{\overline{\overline{\frac{\partial a}{\partial x_j}}^{\sqrt{\alpha}}\overline{\frac{\partial b}{\partial x_j}}^{\sqrt{\alpha}}}^{\sqrt{\ell^2-\alpha}}\right\}\mathrm{d}\alpha. \tag{C14}$$

Then, with an inverse Fourier transform, the formal solution is obtained,

$$\tau_\ell(a,b) = \int_0^{\ell^2}\left[\overline{\overline{\frac{\partial a}{\partial x_j}}^{\sqrt{\alpha}}\overline{\frac{\partial b}{\partial x_j}}^{\sqrt{\alpha}}}^{\sqrt{\ell^2-\alpha}}\right]\mathrm{d}\alpha. \tag{C15}$$

Now the integrand

$$\mathcal{I} = \overline{\overline{\frac{\partial a}{\partial x_j}}^{\sqrt{\alpha}}\overline{\frac{\partial b}{\partial x_j}}^{\sqrt{\alpha}}}^{\sqrt{\ell^2-\alpha}} \tag{C16}$$

may be expanded as a product of filtered quantities plus a generalized second moment,

$$\mathcal{I} = \overline{\frac{\partial a}{\partial x_j}}^{\sqrt{\ell^2-\alpha}}\overline{\frac{\partial b}{\partial x_j}}^{\sqrt{\ell^2-\alpha}} + \left(\overline{\overline{\frac{\partial a}{\partial x_j}}^{\sqrt{\alpha}}\overline{\frac{\partial b}{\partial x_j}}^{\sqrt{\alpha}}}^{\sqrt{\ell^2-\alpha}} - \overline{\frac{\partial a}{\partial x_j}}^{\sqrt{\ell^2-\alpha}}\overline{\frac{\partial b}{\partial x_j}}^{\sqrt{\ell^2-\alpha}}\right), \tag{C17}$$

with the two successive filters collapsing to a single filter as

$$\mathcal{F}\left\{\overline{\frac{\partial a}{\partial x_j}}^{\sqrt{\alpha}}{}^{\sqrt{\ell^2-\alpha}}\right\} = \exp\left[-\frac{1}{2}k^2(\ell^2-\alpha)\right]\exp\left(-\frac{1}{2}k^2\alpha\right)\mathcal{F}\left\{\frac{\partial a}{\partial x_j}\right\}$$

$$= \exp\left(-\frac{1}{2}k^2\ell^2\right)\mathcal{F}\left\{\frac{\partial a}{\partial x_j}\right\} = \mathcal{F}\left\{\overline{\frac{\partial a}{\partial x_j}}^{\ell}\right\}. \tag{C18}$$

The resulting simplification for the integrand is

$$\mathcal{I} = \overline{\frac{\partial a}{\partial x_j}}^{\ell}\overline{\frac{\partial b}{\partial x_j}}^{\ell} + \tau_\beta\left(\overline{\frac{\partial a}{\partial x_j}}^{\sqrt{\alpha}}, \overline{\frac{\partial b}{\partial x_j}}^{\sqrt{\alpha}}\right), \tag{C19}$$

where $\beta = \sqrt{\ell^2-\alpha}$. The first term on the right is independent of α so may be directly integrated, giving the formal solution,

$$\tau_\ell(a,b) = \ell^2\overline{\frac{\partial a}{\partial x_j}}^{\ell}\overline{\frac{\partial b}{\partial x_j}}^{\ell} + \int_0^{\ell^2}\tau_\beta\left(\overline{\frac{\partial a}{\partial x_j}}^{\sqrt{\alpha}}, \overline{\frac{\partial b}{\partial x_j}}^{\sqrt{\alpha}}\right)\mathrm{d}\alpha. \tag{C20}$$

For the present context, we take $a = u_i$ and $b = u_j$ from the velocity vector and define the velocity gradient tensor, $A_{ij} = \partial u_i/\partial x_j$,

$$\tau_\ell(u_i,u_j) = \ell^2\bar{A}_{ik}^{\ell}\bar{A}_{jk}^{\ell} + \int_0^{\ell^2}\tau_\beta(\bar{A}_{ik}^{\sqrt{\alpha}}, \bar{A}_{jk}^{\sqrt{\alpha}})\,\mathrm{d}\alpha. \tag{C21}$$

Finally, constructing the local cascade rate, $\Pi^\ell = -\tau_\ell(u_i,u_j)\bar{S}_{ij}^{\ell}$, by contracting with the filtered strain-rate tensor,

$$\Pi^\ell = -\ell^2\bar{S}_{ij}^{\ell}\bar{A}_{ik}^{\ell}\bar{A}_{jk}^{\ell} - \bar{S}_{ij}^{\ell}\int_0^{\ell^2}\tau_\beta(\bar{A}_{ik}^{\sqrt{\alpha}}, \bar{A}_{jk}^{\sqrt{\alpha}})\,\mathrm{d}\alpha. \tag{C22}$$

Applying the decomposition of the filtered velocity gradient into filtered strain rate and filtered rotation rate, $\bar{\boldsymbol{A}} = \bar{\boldsymbol{S}} + \bar{\boldsymbol{\Omega}}$,

$$\bar{S}_{ij}^{\ell}\bar{A}_{ik}^{\ell}\bar{A}_{jk}^{\ell} = \bar{S}_{ij}^{\ell}(\bar{S}_{ik}^{\ell}+\bar{\Omega}_{ik}^{\ell})(\bar{S}_{jk}^{\ell}+\bar{\Omega}_{jk}^{\ell}) = \bar{S}_{ij}^{\ell}\bar{S}_{ik}^{\ell}\bar{S}_{jk}^{\ell} + \bar{S}_{ij}^{\ell}\bar{\Omega}_{ik}^{\ell}\bar{S}_{jk}^{\ell} + \bar{S}_{ij}^{\ell}\bar{S}_{ik}^{\ell}\bar{\Omega}_{jk}^{\ell} + \bar{S}_{ij}^{\ell}\bar{\Omega}_{ik}^{\ell}\bar{\Omega}_{jk}^{\ell}, \tag{C23}$$

the middle two terms being zero by symmetry arguments,

$$\bar{S}_{ij}^{\ell}\bar{A}_{ik}^{\ell}\bar{A}_{jk}^{\ell} = \bar{S}_{ij}^{\ell}\bar{S}_{ik}^{\ell}\bar{S}_{jk}^{\ell} + \bar{S}_{ij}^{\ell}\bar{\Omega}_{ik}^{\ell}\bar{\Omega}_{jk}^{\ell} = \bar{S}_{ij}^{\ell}\bar{S}_{ik}^{\ell}\bar{S}_{jk}^{\ell} - \tfrac{1}{4}\bar{\omega}_i^{\ell}\bar{S}_{ij}^{\ell}\bar{\omega}_j^{\ell}, \tag{C24}$$

with $\bar{\Omega}_{ij}^{\ell} = -\frac{1}{2}\epsilon_{ijk}\bar{\omega}_k^{\ell}$. A similar decomposition of the integrand in (C22) is

$$\tau_\beta(\bar{A}_{ik}^{\sqrt{\alpha}}, \bar{A}_{jk}^{\sqrt{\alpha}}) = \tau_\beta(\bar{S}_{ik}^{\sqrt{\alpha}}, \bar{S}_{jk}^{\sqrt{\alpha}}) + \tau_\beta(\bar{S}_{ik}^{\sqrt{\alpha}}, \bar{\Omega}_{jk}^{\sqrt{\alpha}}) + \tau_\beta(\bar{\Omega}_{ik}^{\sqrt{\alpha}}, \bar{S}_{jk}^{\sqrt{\alpha}})$$
$$+ \tau_\beta(\bar{\Omega}_{ik}^{\sqrt{\alpha}}, \bar{\Omega}_{jk}^{\sqrt{\alpha}}). \tag{C25}$$

The substitution of these two into (C22) leads to (3.7).

References

Alexakis, A. & Chibbaro, S. 2020 Local energy flux of turbulent flows. *Phys. Rev. Fluids* **5**, 094604.

Aluie, H. & Eyink, G.L. 2009 Localness of energy cascade in hydrodynamic turbulence. II. Sharp spectral filter. *Phys. Fluids* **21** (11), 115108.

Aoyama, T., Ishihara, T., Kaneda, Y., Yokokawa, M., Itakura, K. & Uno, A. 2005 Statistics of energy transfer in high-resolution direct numerical simulation of turbulence in a periodic box. *J. Phys. Soc. Japan* **74** (12), 3202–3212.

Ashurst, W.. T., Kerstein, A.R., Kerr, R.M. & Gibson, C.H. 1987 Alignment of vorticity and scalar gradient with strain rate in simulated Navier–Stokes turbulence. *Phys. Fluids* **30** (8), 2343–2353.

Ballouz, J.G., Johnson, P.L. & Ouellette, N.T. 2020 Temporal dynamics of the alignment of the turbulent stress and strain rate. *Phys. Rev. Fluids* **5**, 114606.

Ballouz, J.G. & Ouellette, N.T. 2018 Tensor geometry in the turbulent cascade. *J. Fluid Mech.* **835**, 1048–1064.

Ballouz, J.G. & Ouellette, N.T. 2020 Geometric constraints on energy transfer in the turbulent cascade. *Phys. Rev. Fluids* **5**, 034603.

Bershadskii, A. 2008 Near-dissipation range in nonlocal turbulence. *Phys. Fluids* **20** (8), 085103.

Betchov, R. 1956 An inequality concerning the production of vorticity in isotropic turbulence. *J. Fluid Mech.* **1** (05), 497–504.

Borue, V. & Orszag, S.A. 1998 Local energy flux and subgrid-scale statistics in three-dimensional turbulence. *J. Fluid Mech.* **366**, 1–31.

Buaria, D., Pumir, A., Bodenschatz, E. & Yeung, P.-K. 2019 Extreme velocity gradients in turbulent flows. *New J. Phys.* **21** (4), 043004.

Buaria, D. & Sreenivasan, K.R. 2020 Dissipation range of the energy spectrum in high Reynolds number turbulence. *Phys. Rev. Fluids* **5** (9), 092601(R).

Buzzicotti, M., Linkmann, M., Aluie, H., Biferale, L., Brasseur, J. & Meneveau, C. 2018 Effect of filter type on the statistics of energy transfer between resolved and subfilter scales from a-priori analysis of direct numerical simulations of isotropic turbulence. *J. Turbul.* **19** (2), 167–197.

Cantwell, B.J. 1992 Exact solution of a restricted Euler equation for the velocity gradient tensor. *Phys. Fluids* **4** (4), 782–793.

Cantwell, B.J. 1993 On the behavior of velocity gradient tensor invariants in direct numerical simulations of turbulence. *Phys. Fluids* **5** (8), 2008–2013.

Carbone, M. & Bragg, A.D. 2020 Is vortex stretching the main cause of the turbulent energy cascade? *J. Fluid Mech.* **883**, R2.

Cardesa, J.I., Vela-Martín, A., Dong, S. & Jiménez, J. 2015 The temporal evolution of the energy flux across scales in homogeneous turbulence. *Phys. Fluids* **27** (11), 111702.

Chan, W.H.R, Johnson, P.L. & Moin, P. 2020*a* The turbulent bubble break-up cascade. Part 1. Theoretical developments. *J. Fluid Mech.* **912**, A42.

Chan, W.H.R., Johnson, P.L., Moin, P. & Urzay, J. 2020*b* The turbulent bubble break-up cascade. Part 2. Numerical simulations of breaking waves. *J. Fluid Mech.* **912**, A43.

Chen, S., Doolen, G., Herring, J.R., Kraichnan, R.H., Orszag, S.A. & She, Z.S. 1993 Far-dissipation range of turbulence. *Phys. Rev. Lett.* **70**, 3051–3054.

Chen, S., Ecke, R.E., Eyink, G.L., Rivera, M., Wan, M. & Xiao, Z. 2006 Physical mechanism of the two-dimensional inverse energy cascade. *Phys. Rev. Lett.* **96**, 084502.

Chong, M.S., Soria, J., Perry, A.E., Chacin, J., Cantwell, B.J. & Na, Y. 1998 Turbulence structures of wall-bounded shear flows found using DNS data. *J. Fluid Mech.* **357**, 225–247.

Chorin, A.J. 1988 Scaling laws in the vortex lattice model of turbulence. *Commun. Math. Phys.* **114** (1), 167–176.

Clark, R.A., Ferziger, J.H. & Reynolds, W.C. 1979 Evaluation of subgrid-scale models using an accurately simulated turbulent flow. *J. Fluid Mech.* **91** (part 1), 1–16.

Constantin, P., E, W. & Titi, E.S. 1994 Onsager's conjecture on the energy conservation for solutions of Euler's equation. *Commun. Math. Phys.* **165** (1), 207–209.

Danish, M. & Meneveau, C. 2018 Multiscale analysis of the invariants of the velocity gradient tensor in isotropic turbulence. *Phys. Rev. Fluids* **3**, 044604.

Doan, N.A.K., Swaminathan, N., Davidson, P.A. & Tanahashi, M. 2018 Scale locality of the energy cascade using real space quantities. *Phys. Rev. Fluids* **3**, 084601.

Domaradzki, J.A. & Carati, D. 2007*a* An analysis of the energy transfer and the locality of nonlinear interactions in turbulence. *Phys. Fluids* **19** (8), 085112.

Domaradzki, J.A. & Carati, D. 2007*b* A comparison of spectral sharp and smooth filters in the analysis of nonlinear interactions and energy transfer in turbulence. *Phys. Fluids* **19** (8), 085111.

DOMARADZKI, J.A., TEACA, B. & CARATI, D. 2009 Locality properties of the energy flux in turbulence. *Phys. Fluids* **21** (2), 025106.

DONG, S., HUANG, Y., YUAN, X. & LOZANO-DURÁN, A. 2020 The coherent structure of the kinetic energy transfer in shear turbulence. *J. Fluid Mech.* **892**, A22.

DONZIS, D.A. & SREENIVASAN, K.R. 2010 The bottleneck effect and the Kolmogorov constant in isotropic turbulence. *J. Fluid Mech.* **657**, 171–188.

ELSINGA, G.E. & MARUSIC, I. 2010 Evolution and lifetimes of flow topology in a turbulent boundary layer. *Phys. Fluids* **22** (1), 015102.

EYINK, G.L. 1995 Local energy flux and the refined similarity hypothesis. *J. Stat. Phys.* **78** (1–2), 335–351.

EYINK, G.L. 2005 Locality of turbulent cascades. *Physica D* **207** (1), 91–116.

EYINK, G.L. 2006 Multi-scale gradient expansion of the turbulent stress tensor. *J. Fluid Mech.* **549**, 159–190.

EYINK, G.L. 2018 Review of the Onsager 'Ideal Turbulence' theory. arXiv:1803.02223.

EYINK, G.L. & ALUIE, H. 2009 Localness of energy cascade in hydrodynamic turbulence. I. Smooth coarse graining. *Phys. Fluids* **21** (11), 115107.

FALKOVICH, G. 1994 Bottleneck phenomenon in developed turbulence. *Phys. Fluids* **6** (4), 1411–1414.

FISCALETTI, D., ELSINGA, G.E., ATTILI, A., BISETTI, F. & BUXTON, O.R.H. 2016 Scale dependence of the alignment between strain rate and rotation in turbulent shear flow. *Phys. Rev. Fluids* **1**, 064405.

FOIAS, C., MANLEY, O. & SIROVICH, L. 1990 Empirical and stokes eigenfunctions and the far-dissipative turbulent spectrum. *Phys. Fluids* A*: Fluid Dyn.* **2** (3), 464–467.

FRISCH, U. 1995 *Turbulence: The Legacy of A. N. Kolmogorov*. Cambridge University Press.

FRISCH, U., KURIEN, S., PANDIT, R., PAULS, W., RAY, S.S., WIRTH, A. & ZHU, J.-Z. 2008 Hyperviscosity, Galerkin truncation, and bottlenecks in turbulence. *Phys. Rev. Lett.* **101**, 144501.

GERMANO, M. 1992 Turbulence: the filtering approach. *J. Fluid Mech.* **238**, 325–336.

GULITSKI, G., KHOLMYANSKY, M., KINZELBACH, W., LUTHI, B., TSINOBER, A. & YORISH, S. 2007 Velocity and temperature derivatives in high-Reynolds-number turbulent flows in the atmospheric surface layer. Part 1. Facilities, methods and some general results. *J. Fluid Mech.* **589**, 57–81.

HILL, R.J. 2001 Equations relating structure functions of all orders. *J. Fluid Mech.* **434**, 379–388.

ISHIHARA, T., KANEDA, Y., YOKOKAWA, M., ITAKURA, K. & UNO, A. 2005 Energy spectrum in the near dissipation range of high resolution direct numerical simulation of turbulence. *J. Phys. Soc. Japan* **74** (5), 1464–1471.

JIMÉNEZ, J. & WRAY, A.A. 1998 On the characteristics of vortex filaments in isotropic turbulence. *J. Fluid Mech.* **373**, 255–285.

JOHNSON, P.L. 2020*a* Energy transfer from large to small scales in turbulence by multi-scale nonlinear strain and vorticity interactions. *Phys. Rev. Lett.* **124**, 104501.

JOHNSON, P.L. 2020*b* Lagrangian dynamics of the tensor diffusivity model for turbulent subfilter stresses. *Center for Turbulence Research Annual Research Briefs*, pp. 167–173.

DE KÁRMÁN, T. & HOWARTH, L. 1938 On the statistical theory of isotropic turbulence. *Proc. R. Soc. Lond.* A **164** (917), 192–215.

KERR, R.M. 1987 Histograms of helicity and strain in numerical turbulence. *Phys. Rev. Lett.* **59**, 783–786.

KHURSHID, S., DONZIS, D.A. & SREENIVASAN, K.R. 2018 Energy spectrum in the dissipation range. *Phys. Rev. Fluids* **3**, 082601.

KOLMOGOROV, A.N. 1941*a* Dissipation of energy in locally isotropic turbulence. *Dokl. Akad. Nauk SSSR* **32**, 16–18.

KOLMOGOROV, A.N. 1941*b* The local structure of turbulence in incompressible viscous fluid for very large Reynolds numbers. *Dokl. Akad. Nauk SSSR* **30**, 299–303.

KRAICHNAN, R.H. 1959 The structure of isotropic turbulence at very high Reynolds numbers. *J. Fluid Mech.* **5** (4), 497–543.

KRAICHNAN, R.H. 1966 Isotropic turbulence and inertial-range structure. *Phys. Fluids* **9** (9), 1728–1752.

KRAICHNAN, R.H. 1971 Inertial-range transfer in two- and three-dimensional turbulence. *J. Fluid Mech.* **47** (3), 525–535.

KRAICHNAN, R.H. 1976 Eddy viscosity in two and three dimensions. *J. Atmos. Sci.* **33** (8), 1521–1536.

KURIEN, S., TAYLOR, M.A. & MATSUMOTO, T. 2004 Cascade time scales for energy and helicity in homogeneous isotropic turbulence. *Phys. Rev.* E **69**, 066313.

LEONARD, A. 1975 Energy cascade in large-eddy simulations of turbulent fluid flows. In *Turbulent Diffusion in Environmental Pollution* (ed. F.N. Frenkiel & R.E. Munn), Advances in Geophysics, vol. 18, pp. 237–248. Elsevier.

LEUNG, T., SWAMINATHAN, N. & DAVIDSON, P.A. 2012 Geometry and interaction of structures in homogeneous isotropic turbulence. *J. Fluid Mech.* **710**, 453–481.

LOHSE, D. & MÜLLER-GROELING, A. 1995 Bottleneck effects in turbulence: scaling phenomena in r versus p space. *Phys. Rev. Lett.* **74**, 1747–1750.

LOZANO-DURÁN, A., HOLZNER, M. & JIMÉNEZ, J. 2016 Multiscale analysis of the topological invariants in the logarithmic region of turbulent channels at a friction Reynolds number of 932. *J. Fluid Mech.* **803**, 356–394.

LUMLEY, J.L. 1992 Some comments on turbulence. *Phys. Fluids* **4** (2), 203–211.

LUND, T.S. & ROGERS, M.M. 1994 An improved measure of strain state probability in turbulent flows. *Phys. Fluids* **6**, 1838–1847.

LUNDGREN, T.S. 1982 Strained spiral vortex model for turbulent fine structure. *Phys. Fluids* **25** (12), 2193–2203.

L'VOV, V. & FALKOVICH, G. 1992 Counterbalanced interaction locality of developed hydrodynamic turbulence. *Phys. Rev.* A **46**, 4762–4772.

MANLEY, O.P. 1992 The dissipation range spectrum. *Phys. Fluids* A*: Fluid Dyn.* **4** (6), 1320–1321.

MENEVEAU, C. 2011 Lagrangian dynamics and models of the velocity gradient tensor in turbulent flows. *Annu. Rev. Fluid Mech.* **43**, 219–245.

MENEVEAU, C. & KATZ, J. 2000 Scale-invariance and turbulence models for large-eddy simulation. *Annu. Rev. Fluid Mech.* **32** (1), 1–32.

MEYERS, J. & MENEVEAU, C. 2008 A functional form for the energy spectrum parametrizing bottleneck and intermittency effects. *Phys. Fluids* **20** (6), 065109.

MININNI, P.D., ALEXAKIS, A. & POUQUET, A. 2006 Large-scale flow effects, energy transfer, and self-similarity on turbulence. *Phys. Rev.* E **74**, 016303.

MININNI, P.D., ALEXAKIS, A. & POUQUET, A. 2008 Nonlocal interactions in hydrodynamic turbulence at high Reynolds numbers: the slow emergence of scaling laws. *Phys. Rev.* E **77**, 036306.

MISRA, A. & PULLIN, D.I. 1997 A vortex-based subgrid stress model for large-eddy simulation. *Phys. Fluids* **9** (8), 2443–2454.

MONIN, A.S. & YAGLOM, A.M. 1975 *Statistical Fluid Mechanics: Mechanics of Turbulence*. Dover.

MULLIN, J.A. & DAHM, W.J.A. 2006 Dual-plane stereo particle image velocimetry measurements of velocity gradient tensor fields in turbulent shear flow. II. Experimental results. *Phys. Fluids* **18** (3), 035102.

NOMURA, K.K. & POST, G.K. 1998 The structure and dynamics of vorticity and rate of strain in incompressible homogeneous turbulence. *J. Fluid Mech.* **377**, 65–97.

NOVIKOV, E.A. 1961 Energy spectrum of turbulent flow in an incompressible fluid. *Dokl. Akad. Nauk. SSSR* **139** (2), 331–334.

OHKITANI, K. & KISHIBA, S. 1995 Nonlocal nature of vortex stretching in an inviscid fluid. *Phys. Fluids* **7** (2), 411–421.

ONSAGER, L. 1949 Statistical hydrodynamics. *Il Nuovo Cimento (1943–1954)* **6** (2), 279–287.

OOI, A., MARTIN, J., SORIA, J. & CHONG, M.S. 1999 A study of the evolution and characteristics of the invariants of the velocity-gradient tensor in isotropic turbulence. *J. Fluid Mech.* **381**, 141–174.

PATTERSON, G.S. & ORSZAG, S.A. 1971 Spectral calculations of isotropic turbulence: efficient removal of aliasing interactions. *The Phys. Fluids* **14** (11), 2538–2541.

PAUL, I., PAPADAKIS, G. & VASSILICOS, J.C. 2017 Genesis and evolution of velocity gradients in near-field spatially developing turbulence. *J. Fluid Mech.* **815**, 295–332.

POPE, S.B. 2000 *Turbulent Flows*. Cambridge University Press.

PORTWOOD, G.D., NADIGA, B.T., SAENZ, J.A. & LIVESCU, D. 2020 Interpreting neural network models of residual scalar flux. *J. Fluid Mech.* **907**, A23.

PULLIN, D.I. & SAFFMAN, P.G. 1994 Reynolds stresses and one-dimensional spectra for a vortex model of homogeneous anisotropic turbulence. *Phys. Fluids* **6** (5), 1787–1796.

PULLIN, D.I. & SAFFMAN, P.G. 1998 Vortex dynamics in turbulence. *Annu. Rev. Fluid Mech.* **30**, 31–51.

QIAN, J. 1984 Universal equilibrium range of turbulence. *Phys. Fluids* **27** (9), 2229–2233.

RICHARDSON, L.F. 1922 *Weather Prediction by Numerical Process*. Cambridge University Press.

SADDOUGHI, S.G. & VEERAVALLI, S.V. 1994 Local isotropy in turbulent boundary layers at high reynolds number. *J. Fluid Mech.* **268**, 333–372.

SANADA, T. 1992 Comment on the dissipation-range spectrum in turbulent flows. *Phys. Fluids* A*: Fluid Dyn.* **4** (5), 1086–1087.

SILVIS, M.H. & VERSTAPPEN, R. 2019 Nonlinear subgrid-scale models for large-eddy simulation of rotating turbulent flows. In *Direct and Large-Eddy Simulation XI* (ed. M.V. Salvetti, V. Armenio, J. Fröhlich, B.J. Geurts & H. Kuerten), pp. 129–134. Springer.

SIROVICH, L., SMITH, L. & YAKHOT, V. 1994 Energy spectrum of homogeneous and isotropic turbulence in far dissipation range. *Phys. Rev. Lett.* **72**, 344–347.

SMITH, L.M. & REYNOLDS, W.C. 1991 The dissipation-range spectrum and the velocity-derivative skewness in turbulent flows. *Phys. Fluids* A*: Fluid Dyn.* **3** (5), 992–994.

SORIA, J., SONDERGAARD, R., CANTWELL, B.J., CHONG, M.S. & PERRY, A.E. 1994 A study of the fine-scale motions of incompressible time-developing mixing layers. *Phys. Fluids* **6** (2), 871–884.

SREENIVASAN, K.R. 1985 On the fine-scale intermittency of turbulence. *J. Fluid Mech.* **151**, 81–103.

TAYLOR, G.I. 1938 Production and dissipation of vorticity in a turbulent fluid. *Proc. R. Soc. Lond.* A **164** (916), 15–23.

TENNEKES, H. & LUMLEY, J.L. 1972 *A First Course in Turbulence*. MIT Press.

TOWNSEND, A.A. 1951 On the fine-scale structure of turbulence. *Proc. R. Soc. Lond.* A **208**, 534–542.

TSINOBER, A. 2009 *An Informal Conceptual Introduction to Turbulence*, 2nd edn. Springer.

TSINOBER, A., KIT, E. & DRACOS, T. 1992 Experimental investigation of the field of velocity gradients in turbulent flows. *J. Fluid Mech.* **242**, 169–192.

VELA-MARTÍN, A. & JIMÉNEZ, J. 2021 Entropy, irreversibility and cascades in the inertial range of isotropic turbulence. *J. Fluid Mech.* **915**, A36.

VIEILLEFOSSE, P. 1982 Perfect incompressible fluids. *J. Phys.* **43**, 837–842.

VIEILLEFOSSE, P. 1984 Internal motion of a small element of fluid in an inviscid flow. *Physica* A **125** (1), 150–162.

VLAYKOV, D.G. & WILCZEK, M. 2019 On the small-scale structure of turbulence and its impact on the pressure field. *J. Fluid Mech.* **861**, 422–446.

VREMAN, B., GEURTS, B. & KUERTEN, H. 1994 Realizability conditions for the turbulent stress tensor in large-eddy simulation. *J. Fluid Mech.* **278**, 351–362.

VREMAN, B., GEURTS, B. & KUERTEN, H. 1996 Large-eddy simulation of the temporal mixing layer using the Clark model. *Theor. Comput. Fluid Dyn.* **8** (4), 309–324.

VREMAN, B., GEURTS, B. & KUERTEN, H. 1997 Large-eddy simulation of the turbulent mixing layer. *J. Fluid Mech.* **339**, 357–390.

WALLACE, J.M. 2009 Twenty years of experimental and direct numerical simulation access to the velocity gradient tensor: what have we learned about turbulence? *Phys. Fluids* **21** (2), 021301.

XIAO, Z., WAN, M., CHEN, S. & EYINK, G.L. 2009 Physical mechanism of the inverse energy cascade of two-dimensional turbulence: a numerical investigation. *J. Fluid Mech.* **619**, 1–44.

XU, H., PUMIR, A. & BODENSCHATZ, E. 2011 The pirouette effect in turbulent flows. *Nat. Phys.* **7** (9), 709–712.

ZHOU, Y. 1993*a* Degrees of locality of energy transfer in the inertial range. *Phys. Fluids* **5** (5), 1092–1094.

ZHOU, Y. 1993*b* Interacting scales and energy transfer in isotropic turbulence. *Phys. Fluids* **5** (10), 2511–2524.